A coupled SPH-DEM model for fluid-structure interaction problems with free-surface flow and structural failure

Ke Wu[1], Dongmin Yang[1,*], Nigel Wright[2]

[1] School of Civil Engineering, University of Leeds, LS2 9JT, UK

[2] Faculty of Technology, De Montfort University, LE1 9BH, UK

Abstract

An integrated particle model is developed to study fluid-structure interaction (FSI) problems with fracture in the structure induced by the free surface flow of the fluid. In this model, the Smoothed Particle Hydrodynamics (SPH) based on the kernel approximation and particle approximation is used to model the fluid domain in accordance with Navier-Stokes equations and the Discrete Element Method (DEM) with a parallel bond model is used to represent the real solid structure through a hexagonal packing of bonded particles. Validation tests have been carried out for the DEM model of the structure with deformation and fracture failure, the SPH model of the fluid and the coupled SPH-DEM model of FSI without fracture, all showing very good agreement with analytical solutions and/or published experimental and numerical results. The simulation results of FSI with fracture indicate that the SPH-DEM model developed is capable of capturing the entire FSI process from structural deformation to structural failure and eventually to post-failure deformable body movement.

Keywords: Discrete Element Method, Smoothed Particle Hydrodynamics, Fluid-Structure Interaction, Free Surface Flow, Fracture

Nomenclature

F	the contact force
K	the stiffness of a particle
U	the contact displacement
V	the contact velocity
μ	the friction coefficient
β	the critical damping ratio
$\bar{\beta}$	the moment-contribution factor
m	the particle mass
ρ	the density of a particle
g	the body force acceleration
x	the position vector of a particle

M	the resultant moment acting on a particle	
I	the principle moment of inertia of a particle	
δ	the element thickness	
ν	Poisson's ratio of the material	
E	Young's modulus of the particles	
$\bar{R}$	the radius of a parallel bond	
A	the cross-sectional area of a parallel bond	
W	the kernel function	
h	the smoothing length for a kernel function	
N	the number of particles within the support domain of a kernel function	
r	the distance between two particles	
k	the constant related to particle search radius	
q	the ratio of distance to smoothing length	
P	the pressure of SPH particles	
c	the speed of sound	
Π	the viscosity term in the SPH governing equations	
R	the anti-clump term in the SPH governing equations	

Superscripts and subscripts

n	the normal component of a vector	
s	the shear component of a vector	
A	particle A in a particle pair	
B	particle B in a particle pair	
i	particle i in a particle pair	
j	particle j in a particle pair	
d	the dashpot in the DEM model	
0	the reference value of a physical variable	
b	the bending moment	
t	The twisting moment	

1. Introduction

Fluid-structure interaction (FSI) is a phenomenon in which a flexible structure suffers pressure from the surrounding fluid flow to give rise to deformation, and conversely, the fluid pressure field and flow is affected by the moveable or deformable structure. As a result, the whole interactive process is repeated continuously until the deformation of solid structure remains unchanged.

FSI is a common engineering problem, for instance, the blade of wind turbine is bent in the flapwise direction due to aerodynamic loading [1], the presence and flow of a red blood cell in capillary or

2

arteriole has a significant effect in understanding its microcirculation and regulation [2], the flow pattern of blood in the heart affects the performance of a heart valve [3], in the event of flooding/landslide-building interaction the flood/rock flow potentially gives rise to the collapse of buildings [4], injected CO_2 interacts with reservoir and caprock underground and the interaction can result in unforeseen leakages [5], and vibration-induced buckling is observed in the carbon nano-tubes (CNTs) when delivering fluid flow [6], among many others. This study is concerned with the FSI process involving free surface flow and structural failure, thus a brief review of existing FSI models and their capability or penitential to model such process is discussed first.

1.1 Current numerical modelling approaches for fluid-structure interaction

FSI problems usually involve flow nonlinearity and multiphysics which are too complex to be solved by analytical methods, and a small number of numerical models have been developed in recent years. Although there are various numerical methods being developed and applied to simulate the separate behaviour of fluid and structure, combined methods for FSI are still limited. The challenge of coupling two methods for FSI largely depends on the nature of their discretisation. Conventional mesh-based methods such as the finite difference method (FDM), the finite element method (FEM) and the finite volume method (FVM) discretise the domain into individual meshes. The reliance on mesh makes the treatment of discontinuities (e.g., wave breaking, cracking and contact/separation) difficult because the path of discontinuities may not coincide with the mesh lines. Remeshing techniques can ensure the discontinuities evolve along the mesh lines but at the expense of reduced computational efficiency and degradation of numerical accuracy. In comparison to conventional mesh-based methods, meshfree (or meshless) methods are intended to approximate mathematic equations in the domain only by nodes without being connected by meshes. If the nodes are particles that carry physical properties (e.g., mass) and the system is simulated by the evolution of the particles' trajectory and the particles' properties, then this type of method is usually called a particle method. Typical particle methods are molecular dynamics (MD), Discrete Element Method (DEM), Smoothed Particle Hydrodynamics (SPH), Immersed Particle Method (IBM) and Lattice Boltzmann Method (LBM). It should be noted that in LBM the particles are only allowed to move along the predefined lattices, so it is in some ways a mesh-based particle method. In the meshfree particle methods of MD, SPH and DEM, a contact detection algorithm as well as an interaction law is required to define the particle interaction. The contact detection algorithm is used to determine whether two particles are interactive, and once they interact, then the interaction law must be used to calculate the interaction forces. In previous research, LBM and SPH are mainly used for simulating fluid flow [7, 8] whilst DEM is mainly used for simulating granular flow [9] and solid fracture [10]. Coupled models like SPH-SPH [11], SPH-DEM [12], IBM [13, 14] and LBM-DEM [15] have been developed for fluid-structure or fluid-particle interactions.

3

As FSI involves two phases, i.e., fluid and solid, the numerical methods for each can be the same or different. As the interface between the fluid and solid structure is evolving in space and time, the numerical models of FSI can be classified as Eulerian-Eulerian, Eulerian-Lagrangian and Lagrangian-Lagrangian. In general, an Eulerian method discretises the space into a mesh and defines the unknown values at the fix points, while a Lagrangian method tracks the pathway of each moving mass point. Communications between the mathematical frameworks for fluid and structure are realised through a fluid-structure interface.

The Eulerian-Eulerian models tend to use an Eulerian FDM to treat both fluid and structure boundaries on fixed meshes to avoid mesh reconstruction. This is able to handle large deformation and free movement of the structure in the fluid as well as the contact between structures. However, this comes at the price of high computational costs and additional discretisation errors since the interface is only tracked implicitly by the solution itself. Special techniques have to be used to link the material points between the reference framework and the current framework [16, 17].

The Eulerian-Lagrangian models solve the Eulerian form of the Navier-Stokes equations for fluid on a fixed grid using a finite volume method, e.g., computational fluid dynamics (CFD), and track the moving body (structure) in a Lagrangian fashion. A typical example is the CFD-FEM model [18-21]. An alternative, the Arbitrary Lagrangian-Eulerian method (ALE), was developed to allow arbitrary motion of grid/mesh points with respect to their frame of reference by taking the convection of these points into account. However, for large translations and rotations of the solid or inhomogeneous movements of the mesh points the fluid elements tend to become ill-shaped, which reflects on the accuracy of the solution. Remeshing, in which the whole domain or part of the domain is spatially rediscretised, is then a common strategy. The process of generating mesh multiple times during a computation can, however, be a very troublesome and time consuming task. In particular the contact of the elastic structure with the boundary is not possible within a monolithic formulation using simple ALE coordinates without remeshing techniques [22].

Even though some remedies have been used to minimise those limitations [23, 24], the features such as large deformation, free surfaces and deformable boundaries are still great challenges in coupled CFD-FEM models and conventional Eulerian-Eulerian methods and Euler-Lagrangian methods can only solve FSI problems where the structure is immersed in the fluid field and deforms without any fracture. On the other hand in the meshfree methods, the identification of free surfaces, moving interfaces and deformable boundaries can be handled straightforwardly [25]. Due to those evident advantages in meshfree methods, some research efforts have been focused on coupling meshfree methods with CFD [12] or FEM [26, 27], and even developing coupled meshfree models such as SPH-SPH [11], SPH-DEM [12, 28, 29] and LBM-DEM [26].

The presence of free surface flow in the concerned FSI problems makes SPH preferred to remain in the coupled model to be developed. Among the above models the coupled SPH-FEM model [30], the coupled SPH-SPH model [11, 31] and the coupled SPH-DEM [12, 28, 29] are Lagrangian-Lagrangian schemes. These models are capable of simulating the free-surface flow and dynamic boundary problems involved in FSI problems, but the kernel functions used in SPH for solid structure lack a physical representation of fracture, not to mention further complications such as the permeation of fluid in the porous or fractured zones of solid structure and the large deformation in FEM is still under numerical challenges. In the coupled SPH-DEM models developed in [12, 28] the structures are treated as rigid bodies thus the interaction between structure and fluid is not fully studied and the deformation and fracture of structure has not been achieved. Even if the structures in FSI problems with free surface flow is represented by SPH or FEM, to the authors' best knowledge, none of those models is capable of dealing with fracture or crack initiation in the structure part during the FSI process.

The FEM as a traditional mesh-based method and its extended versions play an important role in dealing with solid fracture or structural failure problems [32, 33]. Phantom-Node method [34] was also incorporated into FEM through integration of overlapped elements in order to handle crack kinematics, but the crack-tip enrichment is still challenging and its flexibility is comprised when crack growth is the only focus. Therefore coupling FEM with SPH for modelling fluid induced structural failure during the FSI process would become even more challenging.

Another method referred as continuous/discontinuous deformation analysis (CDDA) [35] was developed to account for fracture by employing a link element to connect two adjacent elements as a virtual crack extension. Alternatively, meshfree methods [36, 37] as a promising technique in recent years have been applied in modelling of fracture. The development of test and trial function with a sign function can model cracks with arbitrary movement [14]. Rabczuk [13] used immersed particle method treated in fluid and structure, in which a Kirchhoff–Love shell theory is adopted, to model FSI with crack propagation. A cubic/quartic polynomial basis [38] was used in meshfree particle methods, but without taking the gradient of a kernel function to model cracks the polynomial functions used for solid structure lack a physical representation of fracture unlike the traditional constitutive laws described in solid mechanics. Even though these methods are promising in dealing with fracture, it is difficult to extend them for modelling more complicated Fluid-Particle-Structure Interaction (FPSI) system where the particle-particle interaction, particle-structure interaction and particle-fluid interaction has to be considered.

As another type of meshfree methods, DEM, has recently been successfully applied to model the fracture of solids such as ceramics [10], concrete [39] and even composite materials [40]. The particles in DEM are bonded together and the crack initiation and propagation is treated as the

progressive breakings of bonds. The crack pattern is automatically determined without any need of re-meshing and can be dynamically visualized during the simulation process. DEM model does not require the formulation of complex constitutive laws that are essential in FEM model, while it requires calibration with measured macro-scale results to determine the micro-scale particle and contact parameters that will predict the macro-scale response. Therefore, DEM is practical for studying general features of the statics and dynamics of fracturing, like the crack shape, global structural failure due to the collective behaviour of many interacting cracks as well as the dynamic instability of cracks during their propagation.

1.2 Motivation and objectives

This paper aims to present a new approach based on fully meshfree particle methods of SPH and DEM to handle the FSI problems with free surface flow and/or structural failure. One of the objectives of this research is to develop an advanced FSI model for investigating the failure mechanism of infrastructures (e.g. bridges and buildings) during the flooding events. For example, it is becoming more public concerned that the recent failure of transport bridges (particularly those historic and listed masonry bridges that are still widely in service in the UK) due to flooding have caused enormous impact on local transportation and it is timely and financially costly to get them repaired/rebuilt. Proactive reinforcing or strengthening techniques are thus preferred in order to make the bridges more resistant to the scouring and buoyance effects caused by the flood. To address this problem, interdisciplinary knowledge of geotechnical, hydraulic and structural engineering are required, and it also raises a demand on a robust and reliable computer model to predict the interaction between soil, flood and bridge. Thus a numerical model for fluid-particle-structure (FPSI) interaction would be extremely helpful for assessing the risk of bridge collapse and also assisting the development of dedicated strengthening technique to prevent the failure of the bridge at risk.

The SPH-DEM model presented in this paper is the first step of developing a unified particle model for general FPSI problems in engineering with a principal application in flooding caused bridge failure. The coupled SPH-DEM model will be able to capture either the deformation or the fracture events in the solid structure induced by the free surface flow of the fluid. In this approach, the SPH based on the Navier-Stokes equations is used to model the fluid domain. The DEM is used to represent the solid structure through a dense packing of bonded particles which allows deformation and/or fracture. Similar approaches have already been adopted for modelling ceramics [10] and concrete [41]. As the interaction between discrete particles can be naturally taken into account by DEM, the coupled SPH-DEM presented in this paper for FSI has the potential of being easily extended to model the interaction between fluid, particles and structure simultaneously, and applied to address the FPSI problems in engineering as such discussed above. As both fluid and structure components are represented in the same framework, the coupling between SPH and DEM can be

easily achieved, and more importantly they can be computationally accelerated for large scale simulations by using GPU technique which has been already successful for individual SPH and DEM models. In addition the DEM can deal with discrete particles through contacts as well as continuous structures through bonded particles, thus the coupled SPH-DEM model is applicable to FSI problems and also Fluid-Particle-Structure Interaction (FPSI) problems. The coupled model is first applied in the FSI problems before being extended to the FPSI problems.

This paper is organized as follows: First, individual DEM and SPH models are developed and validated against theoretical and existing numerical/experimental results; An interface model is then proposed to couple the DEM and SPH models, which is then validated against a standard FSI test; Finally, the coupled SPH-DEM model is applied to investigate a more complex FSI problem in which the fracture failure in the structure is allowed due to increasing fluid pressure.

2. DEM model of a structure

The discrete or distinct element method (DEM) was initially proposed by Cundall for studying the discontinuous mechanical behaviour of rock by assemblies of discs and spheres [42]. Upon the development of DEM in recent decades, its applications have been extended in various engineering research fields such as granular flow [39, 40] and fracture of materials and structures including rock [35], ceramics [10], concrete [41] and composites [36], etc. DEM is a Lagrangian method in which the target material is represented by particles that can interact with their neighbours. Every single particle is tracked in DEM throughout the entire time history of simulation, thus the field variables of a particle are updated in every timestep according to the interaction with neighbour particles that are in 'direct' or 'indirect' contact. The contact between two particles in DEM is typically represented by a spring and a dashpot in both normal and tangential directions, as well as a frictional element as shown in Fig.1. By direct contact, the two particles physically touch or overlap with each other. Two particles could be considered as in indirect (or distance) contact when their distance is within certain range [43]. The indirect contact can enable long-range interaction between particles in a way similar to the Van der Waals forces between molecules according to a potential function in Molecular Dynamics (MD). This indirect contact feature will be adopted to account for the interaction between particles within the smoothing length in Smoothed Particle Hydrodynamics (SPH) for the fluid part that will be discussed later. In this section, the structural part will be modelled by DEM using particles in direct contact. It should also be noted that particles in DEM can be rigid or deformable and can have a complex shape, e.g., elliptical. In this paper, 2D rigid particles with a circular shape are considered, and the Particle Flow Code in two dimensions (PFC2D 5.0) is employed as the simulation platform [44].
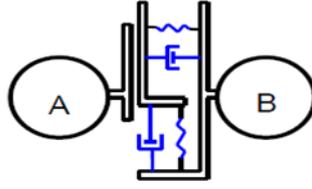
Fig.1 2D representation of contact between two particles in DEM

In a DEM the relative displacement (see Fig.2) between two contacting particles is fed into a force-displacement law to update the contact forces. The calculated contact forces are then applied in the law of motion, Newton's Second Law, to determine the particle's acceleration which is then used to update the particle velocity as well as the particle position. These two laws are applied repeatedly to form the whole calculation cycle of DEM. Therefore, DEM is particularly suitable for simulating the dynamic behaviour of discontinuous system, in which the movement of every particle is recorded and analysed over each time step.
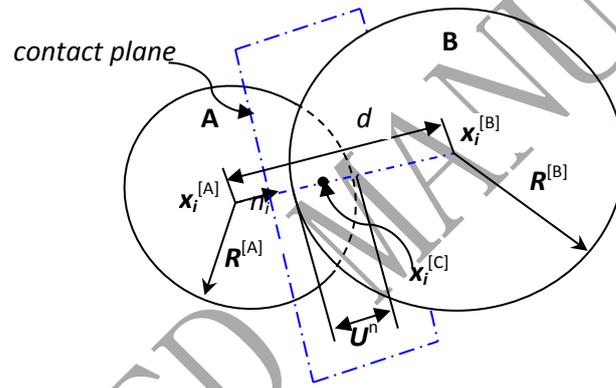
Fig.2 Two particles in direct contact

2.1 Force-displacement law

The force-displacement law for a contact between two particles without the presence of a bond is usually based on contact mechanics theory such as Hertz linear contact theory [45]. When a bond is assigned to the contact, the overall force-displacement of the bonded particles is a combination of particle and bond properties. As fracture of bonds, which could induce pure particle-particle contact on the cracked surfaces, will be allowed in some of the simulations presented in this paper, the force-displacement law for pure particle-particle contact is briefly described first, followed by the constitutive law of the bond. More details are available in the literature [43, 46].

At the contact between two unbonded particles, the contact force vector is further resolved into normal and shear components with respect to the contact plane (see Fig. 2) as follows:

$$F = F^n + F^s \tag{1}$$

where F^n and F^s denote the normal and shear components, respectively.

8

The magnitude of the normal force is the product of the normal stiffness at the contact and the overlap between the two particles, i.e.,

$$F^n = K^n U^n \tag{2}$$

where K^n is the normal stiffness and U^n is the overlap.

The shear force is calculated in an incremental fashion. Initially the total shear force is set to zero upon the formation of contact and then in each timestep the relative incremental shear-displacement is added to the previous value in last timestep:

$$F^s = F^s + \Delta F^s \tag{3}$$
$$\Delta F^s = -K^s \Delta U^s \tag{4}$$
$$\Delta U^s = V^s \Delta t \tag{5}$$

where K^s is the shear stiffness at the contact, ΔU^s is the shear component of the contact displacement, V^s is the shear component of the contact velocity and Δt is the timestep.

In addition, the maximum allowable shear contact force is limited by the slip condition:

$$F^s_{max} = \mu |F^n| \tag{6}$$

where μ is the friction coefficient at the contact.

In cases where a steady-state solution is required in a reasonable number of cycles, the dashpot force acting as viscous damping is grouped into the force-displacement law to account for the compensation of insufficient frictional sliding or no frictional sliding. In line with spring forces, the dashpot force is also resolved into normal and shear components at the contact:

$$F^d_n = 2\beta_n \sqrt{mK_n} \delta_n \tag{7}$$
$$F^d_s = 2\beta_s \sqrt{mK_s} \delta_s \tag{8}$$
$$m = \frac{m_A m_B}{m_A + m_B} \tag{9}$$

where d in superscript denotes dashpot, A and B in subscript denote the two particles in the contact pair, β is the critical damping ratio and δ is the relative velocity difference between two particles in contact.

When a bond is created between two particles, the normal and shear components of the bond force are included in the force-displacement law. It is noted that normal bond force is first examined to see if the tensile-strength limit is exceeded. If a bond is still present in the tension state, the shear-strength limit is enforced for second iteration. When the bond is broken the bond force is diminished in the force-displacement law. Details of the fracture of bonds in DEM will be discussed in Section 2.3.

2.2 Law of motion

9

The motion of each particle in each timestep is governed by Newton's Second Law in terms of translational and rotational motions as follow

Translational motion:
$$F_i = m(\ddot{x}_i - g_i) \tag{10}$$

Rotational motion:
$$M_i = I\dot{\omega}_i \tag{11}$$

where i in subscript is the indicial notation with respect to coordinate system, F_i is the resultant force, m is the total mass of particle, g_i is the body force acceleration vector, $\ddot{x}_i$ is the acceleration vector of a particle, M_i is the resultant moment acting on a particle, I is the principal moment of inertia of the particle, and $\dot{\omega}_i$ is the angular acceleration about the principal axes.

The leap-frog method is used to update the position of the particle. First the relationship between the acceleration and velocity is defined by

$$\ddot{x}_i^{(t)} = \frac{1}{\Delta t}(\dot{x}_i^{\left(t+\frac{\Delta t}{2}\right)} - \dot{x}_i^{\left(t-\frac{\Delta t}{2}\right)}) \tag{12}$$

$$\dot{\omega}_i^{(t)} = \frac{1}{\Delta t}(\omega_i^{\left(t+\frac{\Delta t}{2}\right)} - \omega_i^{\left(t-\frac{\Delta t}{2}\right)}) \tag{13}$$

Then Eqs. (12) and (13) are substituted into Eqs. (10) and (11) respectively and the velocity at time $(t + \frac{\Delta t}{2})$ is resolved as:

$$\dot{x}_i^{\left(t+\frac{\Delta t}{2}\right)} = \dot{x}_i^{\left(t-\frac{\Delta t}{2}\right)} + (\frac{F_i^{(t)}}{m} + g_i)\Delta t \tag{14}$$

$$\omega_i^{\left(t+\frac{\Delta t}{2}\right)} = \omega_i^{\left(t-\frac{\Delta t}{2}\right)} + (\frac{M_i^{(t)}}{I})\Delta t \tag{15}$$

Finally the position of the particle is updated accordingly:

$$x_i^{(t+\Delta t)} = x_i^{(t)} + \dot{x}_i^{\left(t+\frac{\Delta t}{2}\right)}\Delta t \tag{16}$$

2.3 Contact models in DEM

Particles in DEM can be bonded together at contacts and separated when the bond strength or energy is exceeded. Therefore it can simulate the motion of individual particles and also the behaviour of a structure which is formed by assembling many particles through bonds at contacts.

The advantage of DEM is that the two bonded particles can be separated and thus form a crack at the contact point once the fracture criterion of the bond is satisfied. In a DEM model, elementary micro scale particles are assembled to form the structure with macroscopic continuum behaviour determined only by the dynamic interaction of all particles. Unlike the conventional FEM that is based on the traditional continuum mechanics and provides stress and displacement solutions by solving a global stiffness matrix equation, DEM is discontinuous and the information of each particle element and contact is recorded individually and updated dynamically. Thus, DEM is convenient to deal with local

behaviour of a material by defining local models or parameters for the specified particles and contacts. Subject to external loading, when the strength or the fracture energy of a bond between particles is exceeded, flow and disaggregation of the particle assembly occur and the bond starts breaking.

Particles can be packed in a regular (e.g. hexagonal or cubic in 2D) or random form. When they are packed in a hexagonal form in plane stress condition, as shown in Fig.3, the relationship between the elasticity of the constructed structure and the stiffness of the contacts can be derived as [47]:

$$K_n = \frac{E\delta}{\sqrt{3}(1-\nu)} \tag{17}$$

$$K_s = \frac{E\delta(1-3\nu)}{\sqrt{3}(1-\nu^2)} \tag{18}$$

where K_n and K_s are the contact stiffness in normal and shear directions respectively, E is the Young's modulus, δ is the element thickness and ν is the Poisson's ratio.

As illustrated in Eq. (18), there is a constraint of (1-3ν) term on the right-hand side of equation in which the value of Poisson's ratio needs to be smaller than or equal to 0.33 so as to guarantee a positive value of K_s.
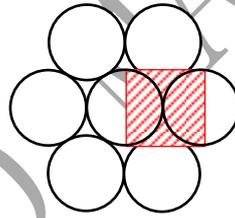
Fig. 3 Hexagonal packing of discrete particles with parallel bonds

A bond in DEM can be regarded as a glue to stick two particles together, and linear parallel bond is special bond (see rectangular box indicated in Fig.3) that can be decomposed into linear model and parallel bond model which are acting in parallel. The bond is broken when the strength limit of bond is exceeded [40, 43] and after that only the linear model is active. Upon the use of a linear parallel bond model, the contact stiffness K_i is the result of combination of both particles' stiffnsess and bond stiffness according to the following formulation [43]:

$$K_i = A\bar{k}_i + k_i \tag{19}$$

$$A = 2\bar{R}\delta \tag{20}$$

$$k_i = \frac{k_i^{[A]}k_i^{[B]}}{k_i^{[A]} + k_i^{[B]}} \tag{21}$$

Where $\bar{R}$ and A are the radius and cross-sectional area of the bond, respectively, $\bar{k}_i$ is the parallel bond stiffness and k_i is the equivalent stiffness of two contacting particles. In this study the radius of the

11

bond is the same as the particle radius. If two particles have the same normal and shear stiffness, k_i is simplified as:

$$k_i = \frac{k_i^{[A]}}{2} = \frac{k_i^{[B]}}{2} \tag{22}$$

It can be assumed that the parallel bond stiffness is much larger than the particles' stiffness, thus the forces are predominantly passed through parallel bonds, i.e. $k_i = 0.01 A \bar{k}_\iota$,

$$K_i \approx A \bar{k}_\iota \tag{23}$$

Thus the parallel bond stiffness is determined by combining Eqs. (19) and (20) with Eq.(23).

According to the nature of parallel bond model, bond strength is the only criterion to determine the fracture of a structure. When the structure is under pure tension, the bond strength can be derived in terms of ultimate tensile strength and Poisson's ratio [41]:

$$f_n^{crit} = \frac{\bar{R}\delta\sigma_{ult}}{2(1-v)}(\sqrt{3} - \frac{v}{\sqrt{3}}) \tag{24}$$

$$f_s^{crit} = \frac{\bar{R}\delta\sigma_{ult}}{2(1-v)}(1 - 3v) \tag{25}$$

$$\sigma_n^{crit} = \frac{f_n^{crit}}{2\bar{R}\delta} \tag{26}$$

$$\sigma_s^{crit} = \frac{f_t^{crit}}{2\bar{R}\delta} \tag{27}$$

where f_n^{crit} and f_s^{crit} are maximum normal and shear forces acting on the parallel bond, σ_n^{crit} and σ_s^{crit} are critical tensile and shear stresses. It should be noted that the above derivation is only valid for 2D simulations in plane stress condition.

During the simulation, the parallel bond forces in normal and shear directions are updated at each timestep through the force-displacement law:

$$f_n = A\bar{k}_n \Delta\delta_n \tag{28}$$

$$f_s = -A\bar{k}_s \Delta\delta_s \tag{29}$$

$$\sigma_n = \frac{f_n}{A} + \bar{\beta}\frac{M_b\bar{R}}{I} = \bar{k}_n\Delta\delta_n + +\bar{\beta}\frac{M_b\bar{R}}{I} \tag{30}$$

$$\sigma_s = \frac{|f_s|}{A} + \begin{cases} 0, (2D) \\ \bar{\beta}\frac{M_t\bar{R}}{I}, (3D) \end{cases} = \bar{k}_s\Delta\delta_s + \begin{cases} 0, (2D) \\ \bar{\beta}\frac{M_t\bar{R}}{I}, (3D) \end{cases} \tag{31}$$

where $\Delta\delta_n$ and $\Delta\delta_s$ are the relative normal-displacement increment and the relative shear-displacement increment respectively, M_b is the bending moment, M_t is the twisting moment and $\bar{\beta}$ is the moment-contribution factor. It should be noted that $\bar{\beta}$ in Eqs. (30) and (31) is set to be zero in order to match those derived formulations in Eqs. (26) and (27).

Then the strength limit is enforced to examine if the gained stresses exceed the threshold value of critical stresses. If the tensile-strength limit is exceeded (i.e. $\sigma_n \geq \sigma_n^{crit}$), then the bond is broken in tension, otherwise, shear-strength limit is enforced subsequently and the bond is broken in shear if $\sigma_s \geq \sigma_s^{crit}$. Once two particles are in unbonded state, parallel bond model is not active any more, but the linear particle-particle contact model, which force-displacement law is described in Section 2.1, is then activated to account for the collision of particles. More details about parallel bond can be found in [43, 46].

As seen from Eqs. (30) and (31), parallel bond is behaved linearly and the plastic deformation is not taken into consideration here. As for plastic or adhesive materials, several alternative models may be used by considering more complicated constitutive behaviour. One of them is the contact softening model [47] which is a bilinear elastic model and is similar to cohesive zone model (CZM) in continuum mechanics. In this study the structure is considered as elastic.

2.3 DEM modelling of structural deformation and fracture

To verify the capability of DEM in modelling the structure part in later FSI simulations, a tip-loaded cantilever beam test is studied in this section. Comparisons of deflections, stress distributions and final failure load are made to carefully evaluate the accuracy of the DEM approach in modelling structural deformation and fracture.

The material properties of cantilever beam are shown in Table 1 and the configuration of the beam is shown in Fig.4. The left end of cantilever is clamped and the other side of cantilever is under an increasing upward force F to give rise to a deflection.

Table.1 the list of material and particle properties

| Material properties	Values
Density, ρ (kg/m³)	2800
Ultimate tensile strength, σ_{ult} (MPa)	310×10^6
Young's modulus, E (N/m²)	70×10^9
Poisson's ratio, v	0.33
Particle radius, R (m)	0.0005
Bond radius, $\bar{R}$ (m)	0.0005
Cantilever length, L (m)	0.201
Cantilever height, h (m)	0.006196

13

0.201 m

0.006196 m

F
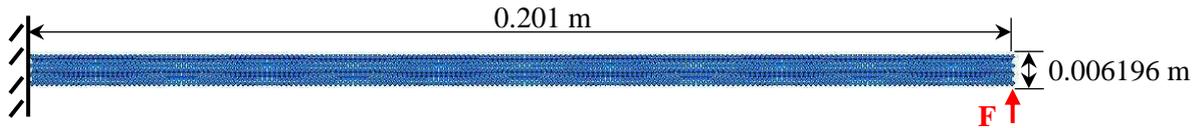
Fig.4 Configuration of cantilever under single point load in DEM

The deformations of cantilever under three sets of upward forces, 50 N, 500 N and 5000 N, applied on the right bottom tip of cantilever are compared with analytical solutions [48] in Table 2. The deflection is measured when the model reaches an equilibrium state that the ratio of the unbalanced force (i.e. the sum of contact force, body force and applied force) to the sum of body force and applied force is extremely small, e.g. 1×10^{-7}. The results from DEM model and analytical solution are almost fully matched with acceptable small errors which may be due to the fact the load is applied at the centre of the particle not the exact edge of the real beam.

Table.2 Deflections for the tip-loaded cantilever beam test

Load (N)	deflection in DEM model (m)	deflection in analytical solution (m)	Error
50	9.7533E-05	1.002417E-05	2.78%
500	9.7533E-04	1.00247E-04	2.78%
5000	9.7533E-03	1.002286E-03	2.76%

In addition, the same test of cantilever beam at load 5000N is carried using FEM software ABAQUS in order to compare the stress distribution. The element size in FEM is the same as the particle radius in DEM. It can be seen from Fig.5 that the distribution of stress component σ_{11} in FEM is nearly identical to the one in DEM. The maximum stresses in both methods are also very close with an error of 0.24%. This further confirms that the DEM model can accurately predict the structural deformation.
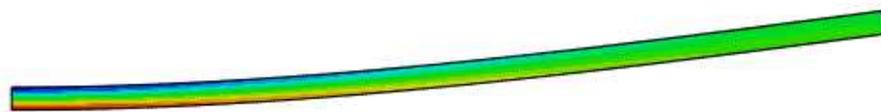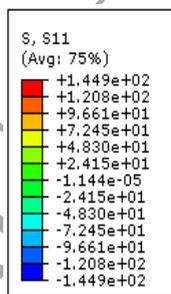
(a) FEM model
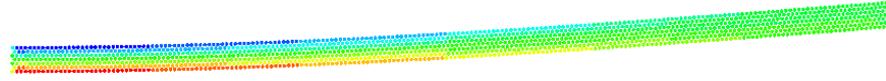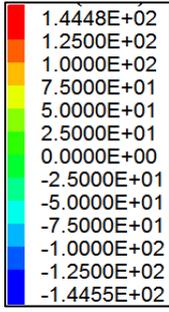
(b) DEM model

Fig.5 Distribution of stress σ_{11} in cantilever beam at load 5000N

To test the failure of the beam, the incremental loading approach used above is replaced by assigning a constant and very small upward velocity $v = 0.02m/s$ to the particle at the right bottom end of the beam. This small loading velocity is chosen to ensure the structure under quasi-static loading condition till the final failure [43]. The simulation is stopped immediately once a bond breaking occurs. The obtained force at right bottom end of the beam is compared with analytical solution according to:

$$\sigma_{ult} = \frac{PL}{Z} \qquad (32)$$

$$Z = \frac{bh^2}{6} \qquad (33)$$

where Z is section modulus, b is the thickness of beam which is unit in 2D simulations. In this test, the cantilever beam is assumed to fail when maximum stress is equal to ultimate tensile strength. In Table. 3 the maximum applied load obtained from the DEM model shows good agreement with the applied load computed from Eqs. (32) and (33). It should be note that the DEM prediction is slightly higher the theoretical one which is calculated under the assumption that the beam is still perfectly straight at failure.

Table. 3 Maximum applied load for the tip-loaded cantilever beam test

	Analytical	DEM	Error
Maximum applied load P (N)	9868.66	10322.1	4.595%

3. SPH model of fluid

Smoothed Particle Hydrodynamics (SPH) is also a Lagrangian particle method which was initially used in astrophysical simulations [49] and later extensively applied in fluid hydrodynamics [50, 51].

The applications of SPH range from multi-phase flow [51], quasi-incompressible flows [52], heat transfer and mass flow [50] and so on.

3.1 Interpolation of a function and interpolation of the derivative of a function

The formulation of SPH is made up of two key steps, kernel approximation and particle approximation. In the first step, the typical integral forms of a function is given by the multiplication of an arbitrary function and a smoothing kernel function, and its derivative are described by simply substituting $f(x)$ with $\nabla \cdot f(x)$ and finally formatted as:

$$f(x) = \int_\Omega f(x')W(x - x', h)dx' \tag{34}$$

$$\nabla \cdot f(x) = \int_S f(x')W(x - x', h) \cdot \vec{n}\, dx' - \int_\Omega f(x') \cdot \nabla W(x - x', h)dx' \tag{35}$$

In the second step, the integral representation of the function and its derivative is approximated by summing up the values of influential surrounding particles and this step is usually called particle approximation, as shown in Fig.6. Only the particles located in the support domain of kernel function with a radius of kh are taken to account in particle approximation. As a result, the final forms of Eqs.(34) and (35) are approximated as:

$$f(x_i) = \sum_{j=1}^N \frac{m_j}{\rho_j} f(x_j)W_{ij} \tag{36}$$

$$\nabla \cdot f(x) = \sum_{j=1}^N \frac{m_j}{\rho_j} f(x_j) \cdot \nabla_i W_{ij} \tag{37}$$

where i and j in subscript denote particle i and j, N is the number of particles within the support domain of the kernel function, m is the mass of the particle and ρ is the density of the particle.
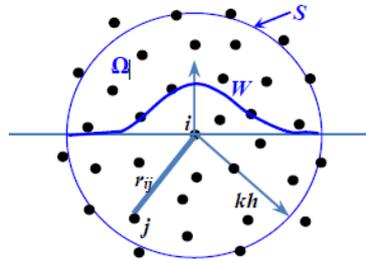
Fig.6 Particle approximations for particle i within the support domain kh of the kernel function W. r_{ij} is the distance between particle i and j, s is the surface of integration domain, Ω is the circular integration domain, k is the constant related to kernel function and h is the smooth length of kernel function.

SPH is adaptive as the field variable approximation is performed at each timestep based on a current local set of arbitrarily distributed particles. Because of this adaptive nature, the formulation of SPH is not affected by the arbitrariness of particle distribution. Therefore, it is attractive in treating large deformations, tracking moving interfaces or free surfaces, and obtaining the time dependent field variables like density, velocity and energy.

3.2 Kernel

Up to now, various kernel functions have been developed and used in the SPH method [25], among which the most widely used are the cubic spline kernel function [53] and the Wendland kernel function [54].

Cubic spline $\quad -W(r,h) = C_h \begin{cases} (2-q)^3 - 4(1-q)^3 & \text{for } 0 \leq q \leq 1 \\ (2-q)^3 & \text{for } 1 < q \leq 2 \\ 0 & \text{for } q > 2 \end{cases}$ (38)

where $q = |r|/h$. $|r|$ is the distance between two particles, h is the smoothing kernel length associated with a particle and the normalisation is ensured by setting up the constant C_h to be $15/(14\pi h^2)$ in two dimensions.

Wendland $\quad W(r,h) = C_h \begin{cases} (2-q)^4(1+2q) & \text{for } 0 \leq q \leq 2 \\ 0 & \text{for } q > 2 \end{cases}$ (39)

where C_h in two dimensions is normalised to be $7/(64\pi h^2)$

Static tank tests are carried out using SPH with both kernel functions. According to the results shown in later section, the simulation using Wendland kernel show more orderly distribution of particle than cubic spline kernel, as a result, the Wendland kernel is chosen for all simulations in this study.

3.3 SPH modelling of incompressible fluid flow

With the application of SPH, Navier-Stokes equations in the form of partial differential equations (PDEs) were transformed into ordinary differential equations (ODEs) through kernel approximation and particle approximation.

For continuity equation, the rate of change of density, in Navier-Stokes form is given by:

$$\frac{D\rho}{Dt} = -\rho \nabla \cdot v$$ (40)

In SPH form, the continuity equation becomes:

$$\frac{D\rho_i}{Dt} = \sum_{j=1}^{N} m_j v_{ij} \frac{\partial W_{ij}}{\partial x_i^\beta}$$ (41)

17

In addition, the density of particle can be directly calculated by summing up all the particles' mass together since the integration of density over the entire problem domain is exactly the total mass of all the particles:

$$\rho_i = \sum_{j=1}^{N} m_j W_{ij} \qquad (42)$$

However, the summation density approach is influenced by the boundaries where the domain of the kernel function is partly truncated, and the non-zero surface integral is directly the result of truncation. One of the accuracy improvements has been proposed to normalise Eq. (42) by summing up the kernel function over the surrounding particles [55]:

$$\rho_i = \frac{\sum_{j=1}^{N} m_j W_{ij}}{\sum_{j=1}^{N} (\frac{m_j}{\rho_j}) W_{ij}} \qquad (43)$$

In concern with the discontinuity at boundary or interface, the density integrated by $\frac{D\rho_i}{Dt}$ can assure the preservation of discontinuity all the time with much less computational cost. Therefore, continuity density approach is the default one to calculate particle density.

Before solving the momentum equations, the inclusive pressure term should be calculated to account for the artificial compressibility assumed in the incompressible flow. In the SPH method, each particle is driven by a pressure gradient which is based on local particle density through an equation of state. However, there is no equation of state for incompressible flow in which the pressure is obtained through continuity and momentum equations. In order to calculate the pressure term in the momentum equations in incompressible flows, the concept of artificial compressibility was proposed to consider what is theoretically an incompressible fluid as weakly compressible fluid [52]. A feasible quasi-incompressible Tait equation of state for incompressible flow is applied as follows:

$$P = B\left(\left(\frac{\rho}{\rho_0}\right)^{\gamma} - 1\right) \qquad (44)$$

where γ is a constant taken to be 7 in most circumstances, ρ_0 is the reference density and B is the pressure constant. The subtraction of 1 on the right-hand side of Eq.(44) is to remove the boundary effect for free surface flow [25].

The value of pressure constant is important to keep the density fluctuation as small as possible. The density fluctuation can be defined as:

$$\frac{|\rho - \rho_0|}{\rho_0} \approx M^2 \equiv \frac{v_{max}^2}{c_s^2} \qquad (45)$$

where M is the Mach number, v_{max} is the maximum velocity and c_s is the speed of sound.

The formulation of the speed of sound at reference density is:

$$c_s{}^2 = \frac{\gamma B}{\rho_0} \tag{46}$$

If the speed of sound is assumed to be 10 times of the maximum velocity, the pressure constant can be worked out then:

$$B = \frac{100\rho_0}{\gamma} v_{max}{}^2 \tag{47}$$

In the same way as the transformation of continuity equation from Navier-Stokes form to SPH form, the moment equation in SPH form is described as:

$$\frac{dv_i}{dt} = \sum_{j=1}^{n} m_j (\frac{P_i}{\rho_i^2} + \frac{P_j}{\rho_j^2} + \Pi_{ij}) \nabla W_{ij} \tag{48}$$

where Π_{ij} is the viscosity term.

There is a wide variety of derivation of the viscosity term [56], and the first one derived as an artificial viscosity is based on the consideration of strong shocks [57]:

$$\Pi_{ij} = \begin{cases} \dfrac{-\alpha c \bar{\mu}_{ij} + \beta \bar{\mu}_{ij}^2}{\bar{\rho}_{ij}} & if \ v_{ij} \cdot r_{ij} < 0 \\ 0 & otherwise \end{cases} \tag{49}$$

where α and β denotes the artificial viscosity coefficient respectively, $\bar{\mu}_{ij} = 1/2(\mu_i + \mu_j)$ and $\bar{\rho}_{ij} = 1/2(\rho_i + \rho_j)$. As it has been a common practice to use an artificial viscosity in compressible SPH formulations for better accuracy in the simulation of shock wave, this viscosity form will not be taken into consideration here. Instead, another viscosity form including physical viscosity of particle derived in [58] is adopted in this study:

$$\Pi_{ij} = m_j \frac{(\mu_i + \mu_j) r_{ij} \cdot \nabla W_{ij}}{\rho_i \rho_j (r_{ij}{}^2 + 0.01h^2)} v_{ij} \tag{50}$$

where $0.01h^2$ in the denominator is meant to avoid singularity.

Apparently Eq.(50) can approximate the viscosity term physically and it is also useful for dealing with multiphase problems where densities at interface are not identical. This will become more important when discrete particles are incorporated in the present SPH-DEM model in the future to enable the FPSI simulations.

3.4 Completeness and tensile instability

Even though SPH is an increasingly promising numerical method, several difficulties have been encountered in recent decades. The first difficulty is the completeness of SPH which is the ability of the approximation to reproduce specified functions and other ones are the rank deficiency and the

19

tensile instability that manifests itself as a bunching of nodes. This unphysical phenomenon, which is normally due to tensile instability, could reduce resolution and even cause numerical errors during the simulation. To extend applications of SPH into a wide range of fluid dynamics problems, a series of modifications and corrections have been introduced to improve the approximation accuracy.

In terms of completeness, there are two approaches for approximating the continuity equation: one is density summation approach and the other one is continuity density approach. The density summation approach conserves the mass since the integration of density over the entire support domain is equal to the total mass of all the particles. However, this approach suffered edge effect, namely boundary particle deficiency where the support domain is not fully filled with particle at the edge of fluid domain, as a result, the density is smoothed out to cause some spurious results. Randles and Libersky [59] proposed the normalisation of the summation density approach with the SPH summation of the smoothing function itself over the surrounding particles to improve the accuracy of approximation. In this study, the continuity density approach was applied instead of the density summation approach to introduce velocity difference into the discrete particle approximation as the usage of the relative velocities in anti-symmetrized form serves to reduce errors arising from the particle inconsistency problem [25].

The rank-deficiency is defined as that the number of integration points is less enough so that the solution to the underlying equilibrium equation becomes non-unique. Even though some researchers [60, 61] proposed to eliminate the rank-deficiency by introducing additional integration points (e.g. stress points) at other locations than the SPH centroids, the increased computational effort associated with the additional integration points renders this approach less efficient, and a precise guideline as to how many additional stress points are needed is missing. In this study, several smooth lengths were tested to find out the optimal value of smooth length in order to keep the rank deficiency as minimum as possible.

The original updated Lagrangian formulation of SPH, which is also termed Eulerian SPH, suffers from the so-called tensile instability, in which leads to the clumping of particles. In a Lagrangian formulation the kernel approximation is performed in the initial, undeformed reference coordinates of the material [14]. In the application of Lagrangian kernel, the tensile instability is absent, however, rank deficiency still exists. In this study, the instability can be removed by using an artificial stress which, in the case of fluids, is an artificial pressure. An anti-clump term was introduced to be added into the momentum equations to prevent particles from forming into small clumps due to unwanted attraction [62]:

$$\frac{dv_i}{dt} = \sum_{j=1}^{n} m_j \left(\frac{P_i}{\rho_i^2} + \frac{P_j}{\rho_j^2} + \Pi_{ij} + R_{ij} \right) \nabla W_{ij} \tag{51}$$

$$R_{ij} = \frac{v_{max}^2}{c_s^2} \left| \frac{P_i}{\rho_i^2} + \frac{P_j}{\rho_j^2} \right| (\frac{W_{ij}}{W_{(\Delta P)}})^4 \tag{52}$$

where $v_{max} = \frac{1}{10} c_s$, and ΔP is the initial particle spacing.

Another remedy also applied in this model is to correct the rate of the change of particle position in order to keep particles move orderly in the high speed flow:

$$\frac{dr_i}{dt} = v_i + \varepsilon \sum_j \frac{m_j(v_j - v_i)}{\bar{\rho}_{ij}} W_{ij} \tag{53}$$

where the second term on the right hand side of Eq.(53) is the correction factor, the value of ε is problem-dependent as large ε can slow down the particle velocity unphysically.

3.5 No-slip boundary

When a SPH particle is approaching a boundary (see Fig.7), its support domain overlaps with the problem domain, consequently its kernel function is truncated partially by the boundary and the surface integral is no longer zero. Theoretically only particles located inside the support domain are accounted for in the summation of the particle interaction, but there are no particles existing in the truncated area beyond the solid boundary. Different remedies have been proposed recently to rectify boundary truncation. The normalisation formulation of density approximation was derived to satisfy the normalisation condition and ensures the integral of kernel function over the support domain is unity [55]. In comparison with kernel re-normalisation, the application of virtual or ghost particles is widely used to replace the solid boundary and to produce a repulsive force in order to avoid wall penetration [52]. The interaction force between a boundary particle and an SPH particle could be in Lennard-Jones form [52], in which the SPH particles are repelled within a cut-off distance, but Lennard-Jones form is highly dependent on the problem being simulated. In order to have a simple, robust as well as reliable, interaction between boundary and SPH particles, in this study two-layers of fixed boundary particles are placed as solid boundaries, which are initialised with a reference density of SPH particles, but their density and other parameters such as position and velocity are all fixed and not evolved with the parameter variance of SPH particles. In order to produce sufficient repulsive forces, the distribution of boundary particles is denser than the distribution of SPH particles as shown in Fig.8.
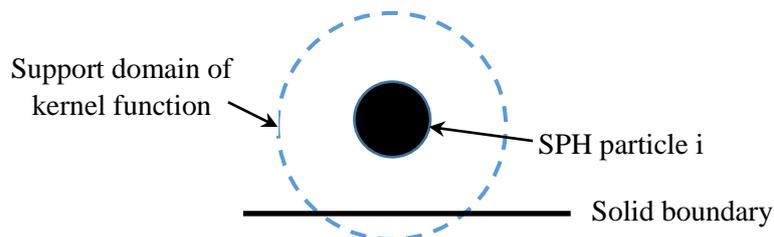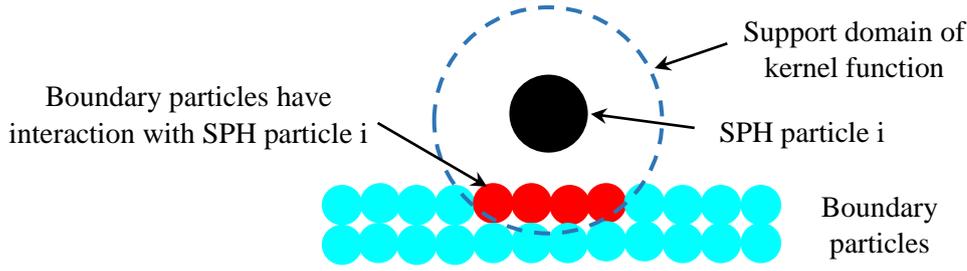
Fig.8 Boundary particles and their interaction with SPH particles

3.6 Smoothing length

Smoothing length can vary in space and time, and this is useful in modelling of compressible flow to ensure the number of particle within kernel is more or less constant. The formulation of smoothing length is:

$$h_i = \sigma(\frac{m_i}{\rho_i})^{1/d} = \sigma\Delta p \qquad (54)$$

where σ is the constant with a typical value of 1.3 and d is the dimensionality of the simulation

As the mass of particle in SPH is assumed to be constant, the smoothing length associated with particle volume should vary accordingly with density. However, the density fluctuation in incompressible flow is minor [63], thus using variable smoothing length with extra computational cost is not expected to produce significantly different results. Therefore, smoothing length is chosen to be constant with $1.25\Delta p$ in this study for easy numerical implementation and saving computational time. Note that it would be better to use variable smooth length to improve the numerical accuracy in the future, however, as a first step in developing this SPH-DEM model, constant smooth length is used for simplicity.

3.7 Numerical implementation of SPH

In this study, the SPH theory above is implemented in PFC2D v5.0 using C++. The indirect contact feature is adopted to enable the particle interaction in SPH. PFC2D 5.0 as a DEM software package which has many features that can be directly utilised for SPH simulations such as a particle search scheme and a time integration scheme. A particle search scheme is based on a Linked-list algorithm to sub-divide the particles within different cells and particles are identified through a linked list. PFC2D 5.0 uses a leapfrog technique for numerical integration to update field variables at each particle. The workload for coding SPH and later SPH-DEM coupling is significantly reduced by making use of those two features. A detailed flow chart of implementing SPH and its coupling with DEM is shown later in this section. As the codes are written in C++, they are portable for other open source DEM codes for SPH-DEM simulations without much modification.

3.8 Sensitivity study and validation of the SPH model

To show the success of implementing SPH into PFC code for modelling the fluid flow in later FSI simulations, the SPH model is carefully assessed through a series of numerical tests including a static tank test to see the performance and adaptability of different kernel functions and a dam break test to evaluate the effects of different smoothing length and particle resolution.

3.8.1   SPH simulation of static tank test with different kernel functions

A simple static stank test with an initial cubic packing of particles is set up in a 30mm × 30mm tank, as shown in Fig.9. Two different kernel functions are investigated, i.e. cubic spline kernel and Wendland kernel. Under only gravity the particle distribution was observed for a time period of 1.0 second.

Each SPH particle is initialised with a hydrostatic pressure in accordance with the particle's position and its reference density. The density of each particle is then updated through equation of state in Eq.(44). The particle spacing Δp is 0.005m and the mass of particle in 2D simulation is described as:

$$m_i = \rho_i (\Delta p)^2$$

(55)

where m_i is the mass of fluid particle.

The smoothing length is initially set as $h = 1.0 \times \Delta p$ for all cases and the maximum velocity of particle is assumed to be $v_{max} = \sqrt{2gD}$, where D is the depth of the fluid and g is the gravitational acceleration, $9.81 m/s^2$. All the material and numerical properties are listed in Table. 4
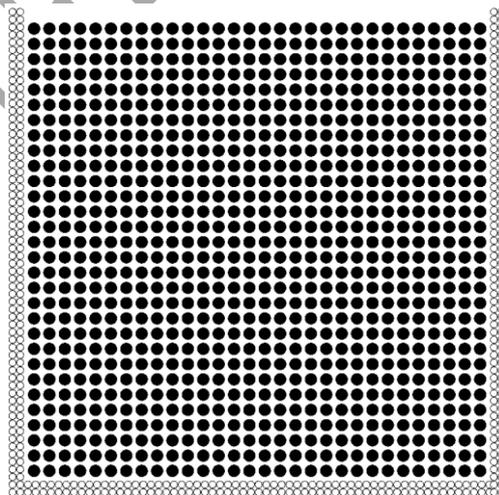

Fig.9 Initial configuration of the static tank test

(SPH particles in black colour and boundary particles in white colour)

Table.4 SPH parameters used for the static tank test

23

Parameters	Values
Boundary particle spacing (m)	0.0025
SPH particle spacing (m)	0.005
Particle number	1278
Kernel function	Cubic spline/Wendland
Kernel smooth length (m)	0.005
Fluid density (kg/m^3)	1000
Fluid viscosity ($Pa \cdot s$)	8.9×10^{-4}
Time step (s)	0.000004
Physical time (s)	1.0

Fig.10 shows the particle distribution at 0.2s time interval for cubic spline kernel and Wendland kernel, respectively. It can be seen that the particle distribution for the test using Wendland kernel nearly remains the same as the original particle distribution and only a small disorder is found at the corners of fluid, which is due to the boundary/interface deficiency. For the test using cubic spline kernel, the particles are packed orderly as well, but the particle distribution is not cubic any more, it and more likely becomes hexagonal after 0.2s. Even though the reason for this difference is not clear, both tests show good particle distribution without any particle cluster. Considering the Wendland kernel seems to produce better form of particle distribution, it will be used for all the simulations later.

Time	Cubic spline kernel	Wendland kernel
(a) t=0.2s		
(b) t=0.4s		
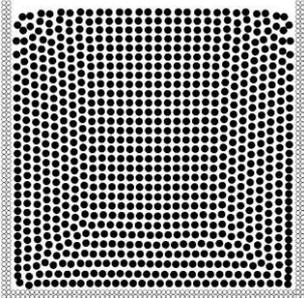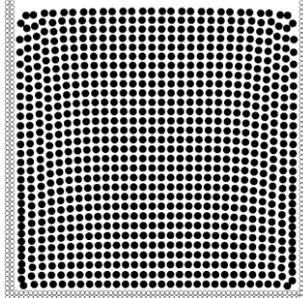
|	
(c) **t=0.6s**	
(d) **t=0.8s**	
(e) **t=1.0s**	
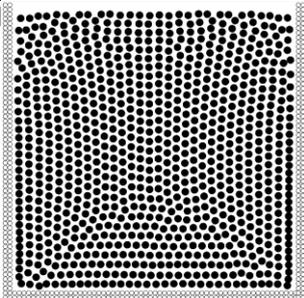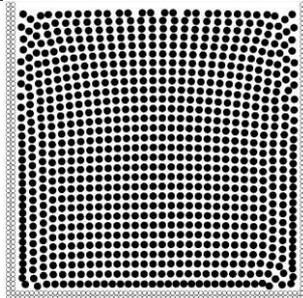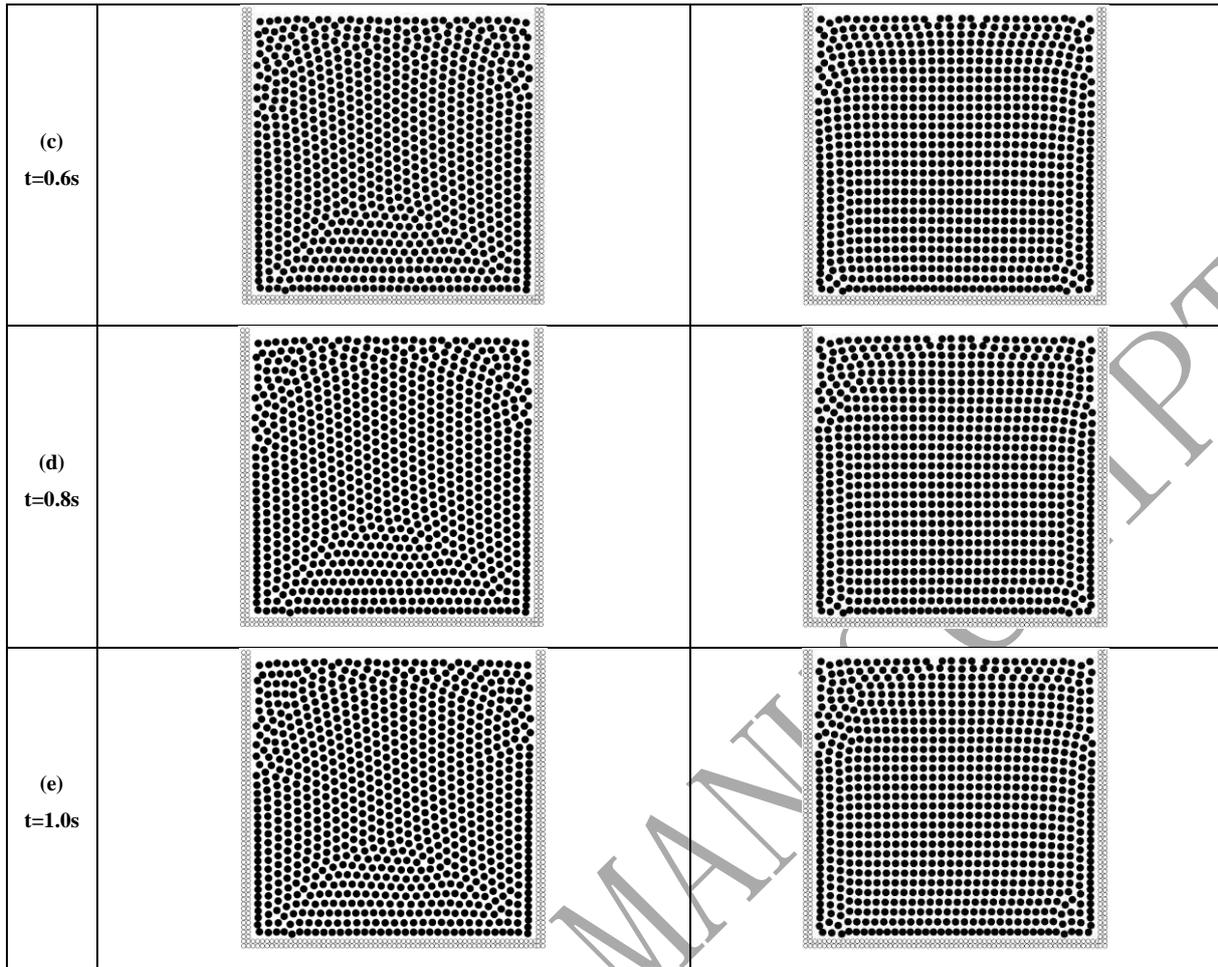
Fig.10 Particle distribution during a period time of 1.0s using two different kernel functions.

3.8.2   SPH simulation of dam break test with different smoothing length

The case of a collapsing water column has been used in SPH studies [64, 65], therefore it is utilised here to validate the implemented SPH model. Besides the validation of SPH model, the effect of different smoothing length, $h = 1.0 \times \Delta p$, $h = 1.25 \times \Delta p$ and $h = 1.5 \times \Delta p$, is also examined. The geometry of the case is depicted in Fig.11 and the simulation parameters are listed in Table 5. The water column is initially adjacent to the left wall and is supported by a wall that is instantaneously removed when the experimental test starts. The water is thereby released into a dry channel. The SPH particles are initialised with hydrostatic pressure in accordance with the position and the density of each SPH particle derived by reversing Eq. (44). The distribution of density for the SPH particles is displayed in Fig. 12.
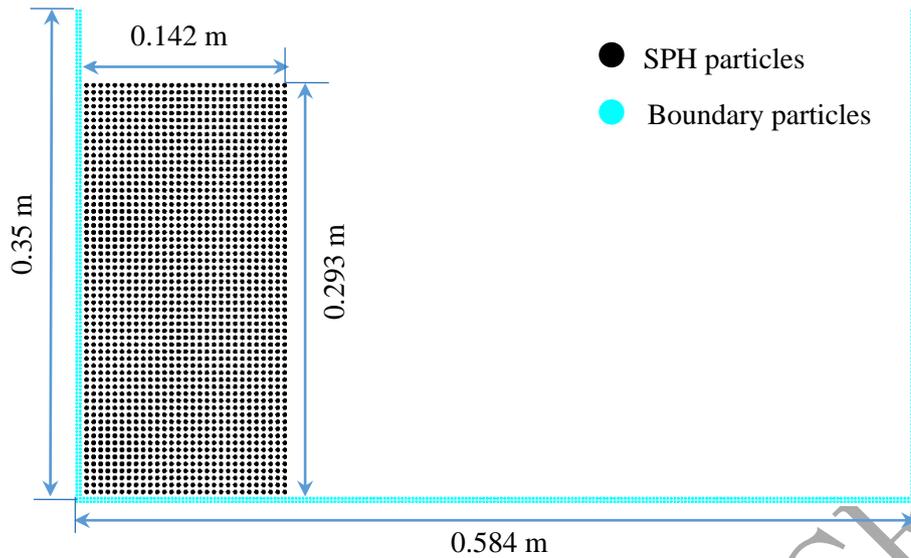
Fig.11 2D SPH representation of the dam-break test
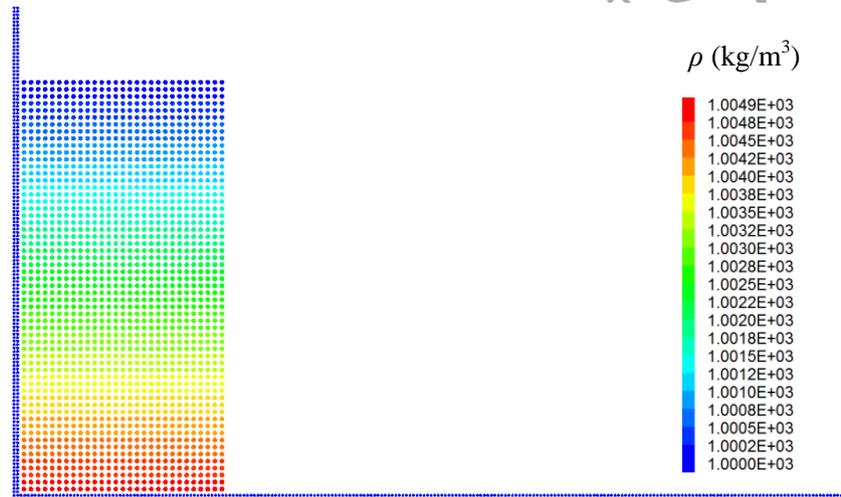
Fig.12 Initial density of SPH particles with an assumption of artificial compressibility

In Fig. 13, the SPH simulation results with a smoothing length of $h = 1.25 \times \Delta p$ are compared with experimental images as well as the numerical simulations using the moving particle semi-implicit method (MPS) for a time period of 1.0s with a time interval of 0.2s [64]. The collapsing water runs along with bottom wall with an increasing velocity at the leading edge at 0.2s (see Fig. 13a), and the accelerated water is then blocked by the right vertical wall thereby moving upwards at 0.4s (see Fig. 13b). At 0.6s, the SPH particles tend to reach the highest position with losing momentum energy which is offset by gravitation acceleration and then these SPH particles fall down to hit other SPH particles which still move along with bottom wall. At 1.0s, the movement of reflected SPH particles is gradually restricted by the left vertical wall. In general all the simulated flow patterns of water in SPH agree well with experiment and MPS.

Fig.14 shows the numerical results with different smoothing length. The flow patterns are almost identical before 0.6s. After 0.6s, those fluid particles repelled back by right vertical wall are gradually mixing with incoming fluid particles that are approaching right vertical wall. Due to this expected phenomenon, the simulations with longer smoothing length can search more surrounding particles to more accurately represent the fluid profile. It is apparent that results with $h = 1.25 \times \Delta p$ and $h = 1.5 \times \Delta p$ showed a good match in fluid profile from the beginning to 1.0s. In addition to the fluid flow profile, computational cost is another determining factor. More computational cost is required for the simulation with $h = 1.5 \times \Delta p$, and it produces better results than $h = 1.0 \times \Delta p$ (particularly at time 1.0s, see Fig.15e) but similar with $h = 1.25 \times \Delta p$. Therefore, smoothing length $h = 1.25 \times \Delta p$ is a better choice for numerical accuracy and computational efficiency and it is chosen for the rest of numerical simulations.

Table.5 SPH parameters for the dam-break test

Parameters	Values
Boundary particle spacing (m)	0.0025
SPH particle spacing (m)	0.005
Particle number	2743
Kernel function	Wendland
Kernel smooth length (m)	0.005/0.00625/0.0075
Fluid density (kg/m^3)	1000
Fluid viscosity (Pa·s)	8.9×10^{-4}
Time step (s)	0.000004
Physical time (s)	1.0

Time	Experiment [66]	MPS [64]	SPH, h=1.25×Δp
(a) t=0.2s			
(b) t=0.4s			

27
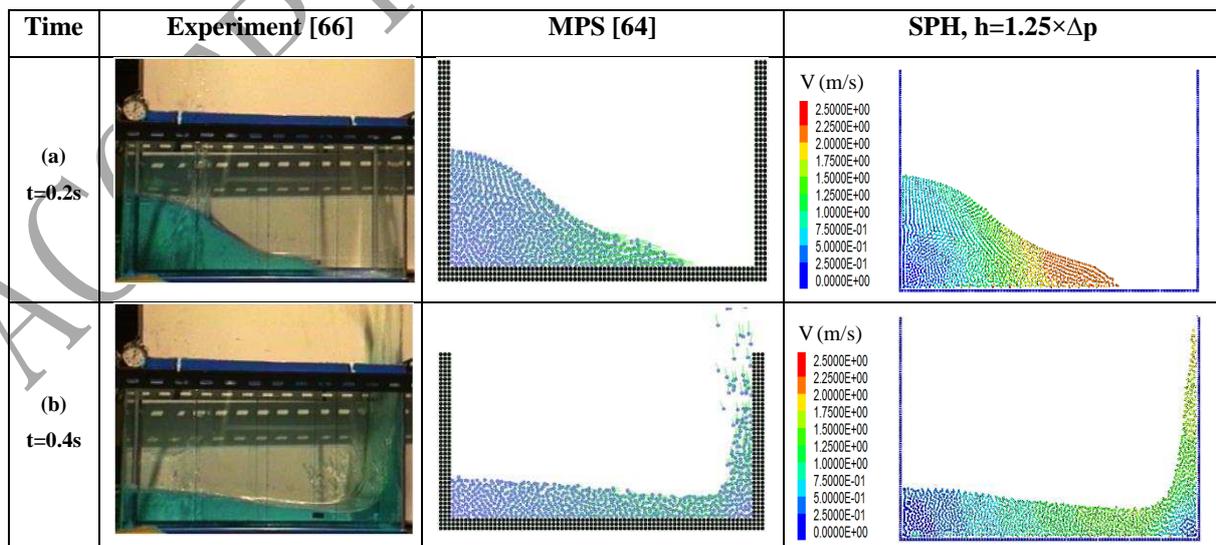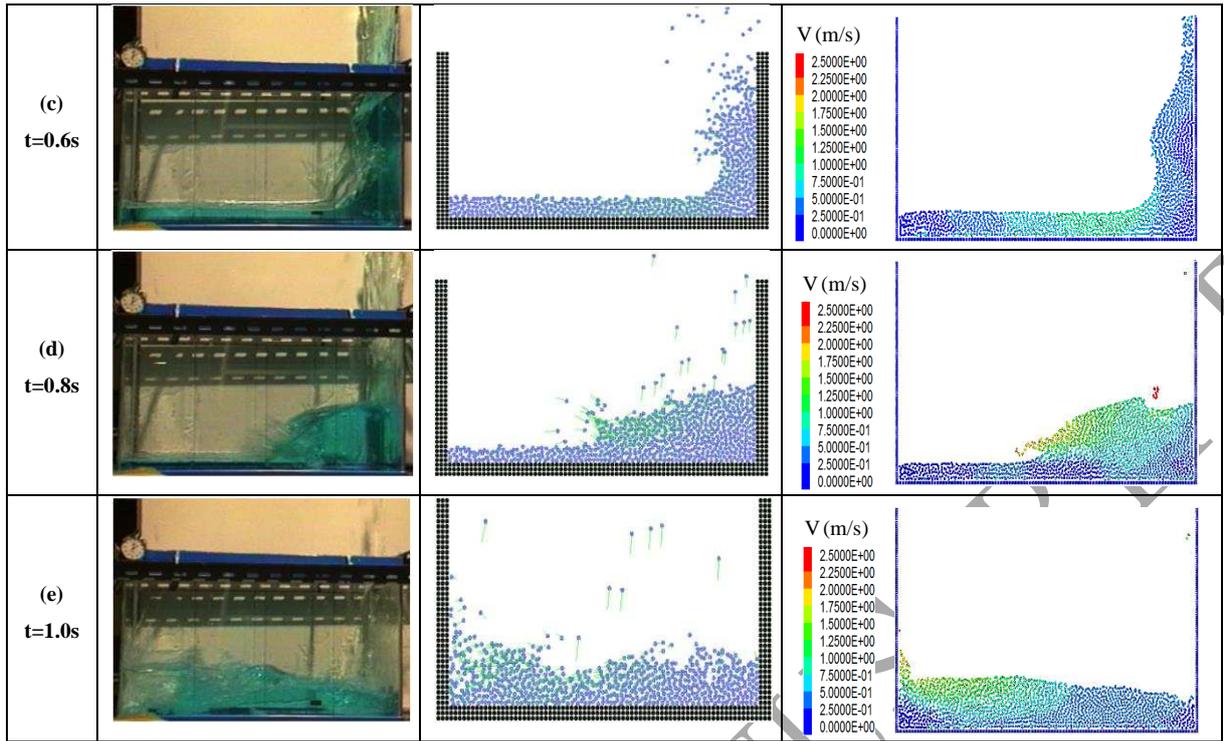
Fig.13 Results from experiment [51], MPS [53] and SPH with **h=1.25×Δp** for a time period of t=1.0s.
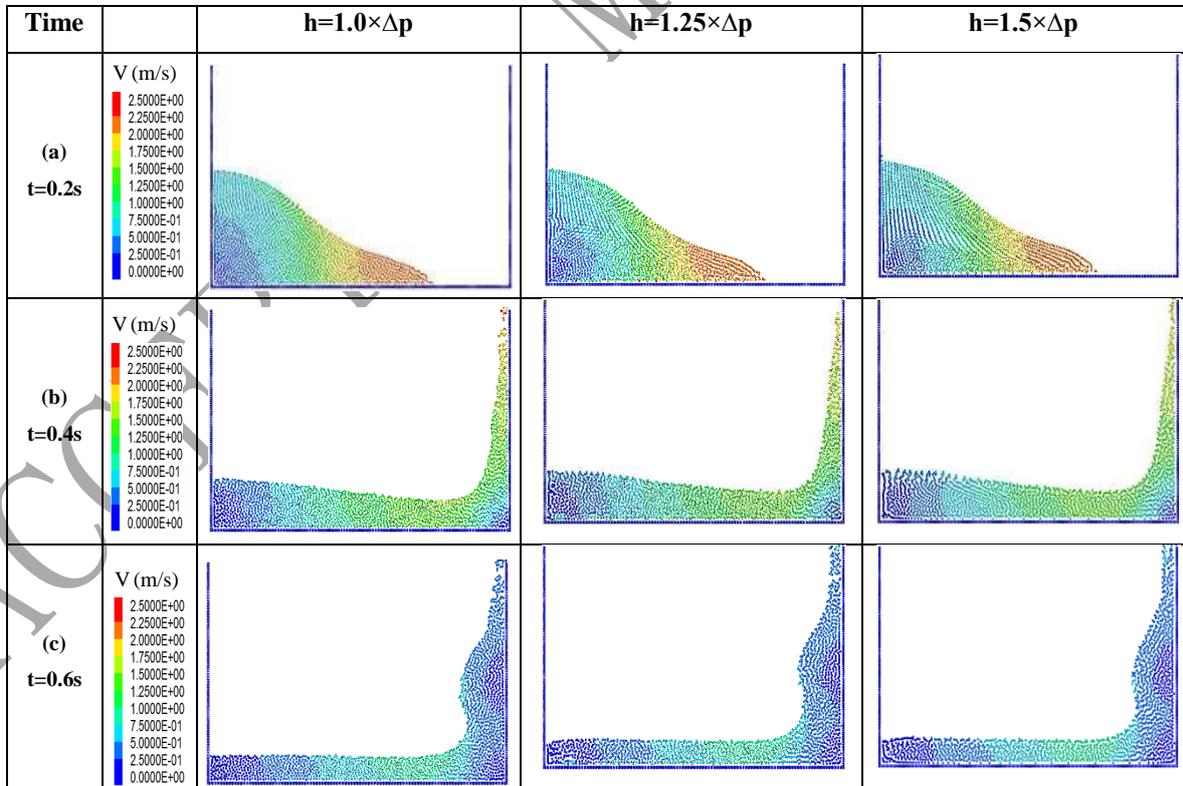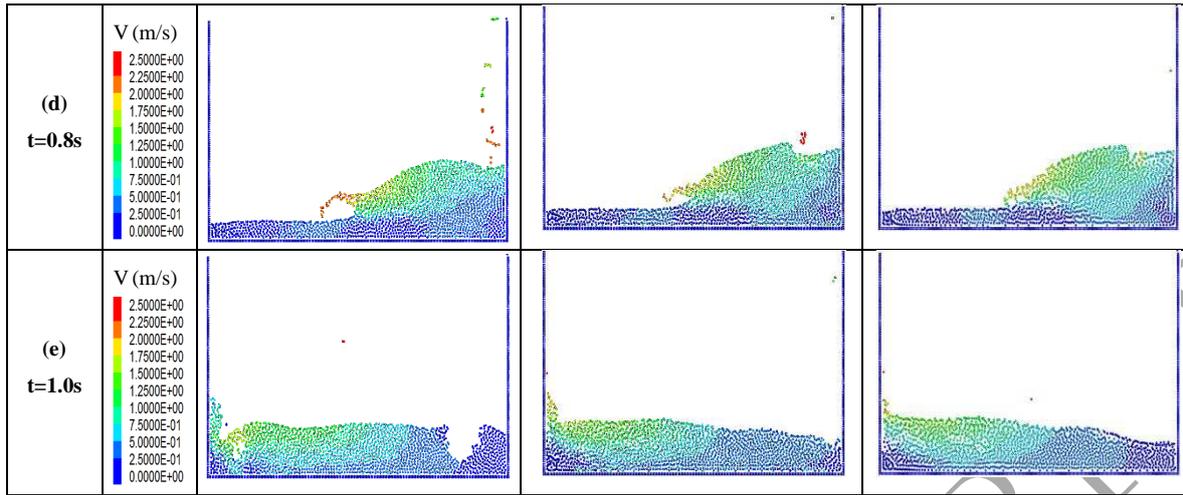
Fig.14 SPH simulations with three different smoothing length for a time period of t=1.0s.

3.8.3   SPH simulation of dam break test with different particle resolutions

In this section the dam break test is simulated again using the same kernel function (Wendland kernel) and smoothing length ($h = 1.25 \times \Delta p$) but three different particle resolutions, i.e. particle spacing Δp. The particle spacing of 0.005m used before is chosen as a sample data, and two more different particle spacing, one is finer whilst the other one is coarser, are investigated for comparisons. The data for three particle resolutions are presented in Table.6, and the simulation results for physical time 1.0s are shown in Fig.15.

Table.6 Particle resolutions in the dam-break test

| Parameters	Coarse	Medium	Fine
Boundary particle spacing (m)	0.003	0.0025	0.002
SPH particle spacing (m)	0.006	0.005	0.004
Particle number	2087	2743	4098
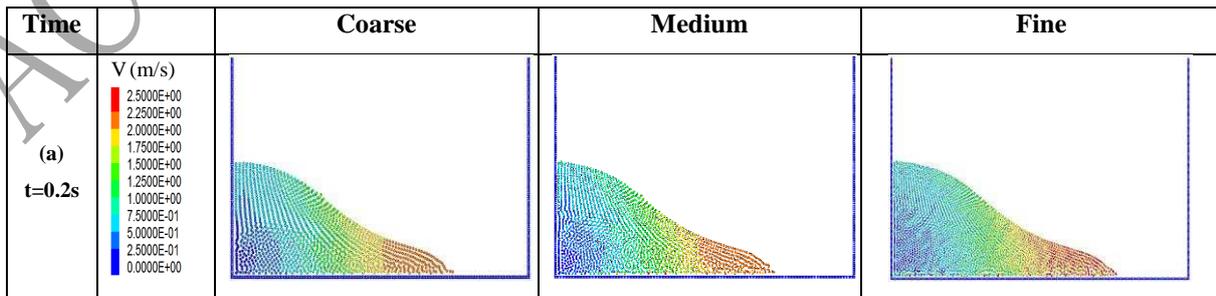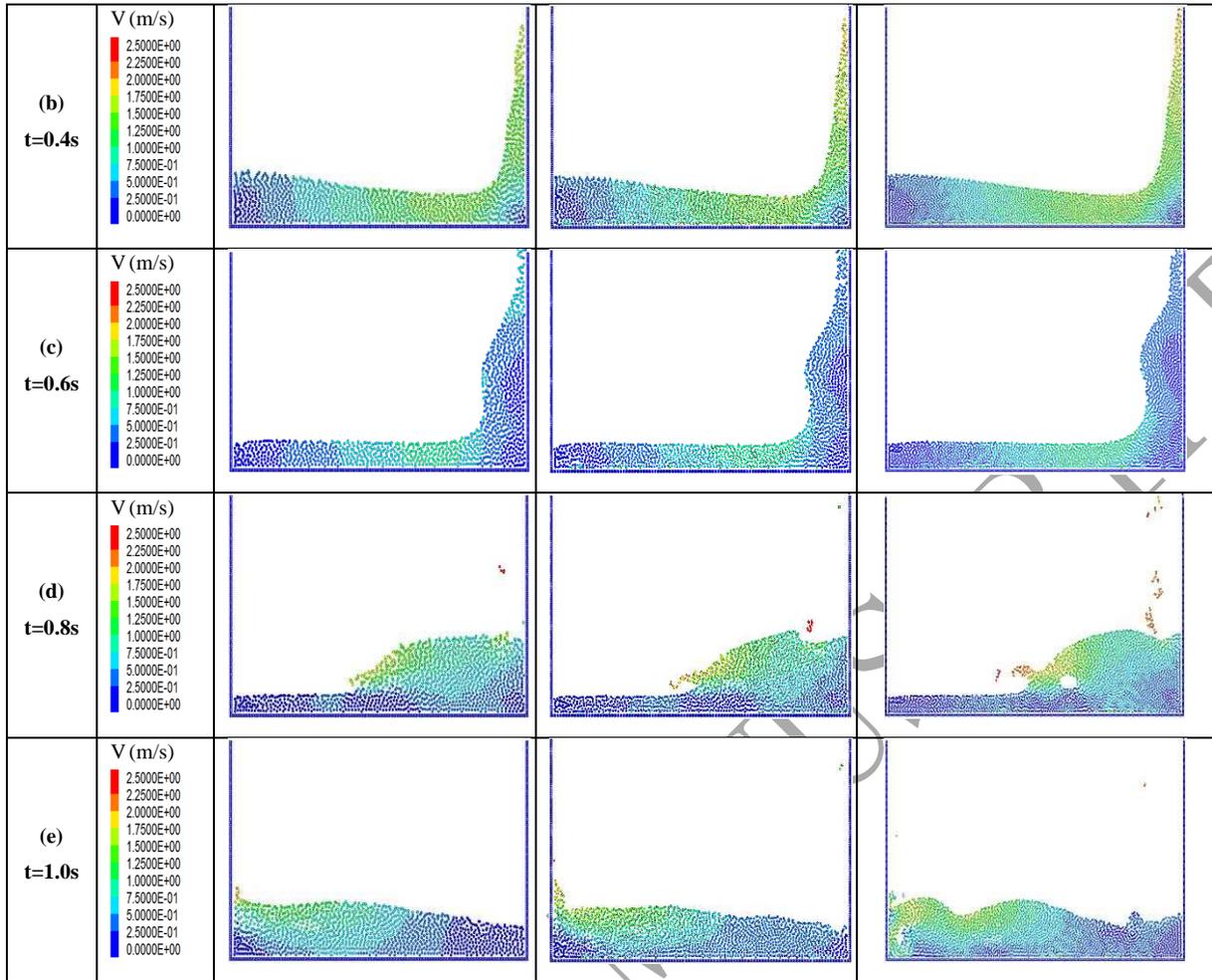
Fig.15 SPH simulations with three different particle resolutions for a time period of t=1.0s.

It is evident in Fig.15 that the results for particle spacing of $\Delta p = 0.004$ show the best fluid flow profile and even capture the void at time $t = 0.8s$ and the curved wave at time $t = 1.0s$. Usually finer particle resolutions would give better results with more fluid flow profile details but at a cost of computational time. Therefore it is essential to balance the numerical accuracy and the computational cost, which highly depends on the kind of results that are expected to achieve. In this study, Wendland kernel and smoothing length in $h = 1.25 \times \Delta p$ are determined to be applied in the following simulation of fluid-structure interaction, and the particle resolution will be adjusted in accordance with the testing problem at a reasonable computational cost.

4. Coupled SPH-DEM model for FSI

4.1 Methodology

In dealing with interface between SPH and DEM particles, the interactive force could be defined differently in accordance with flow configurations (e.g. fluid-structure interaction flow or fluid-particle interaction flow). In the fluid-particle system, the force acting on a single DEM particle is the summation of DEM-DEM contact force, drag force, buoyancy force and gravity force [29, 67].

Conversely, as DEM particles are bonded together in fluid-structure system, the interaction force between SPH and DEM particles can be determined by Newton's Third Law of Motion under a non-slip condition [12, 68]. In this study of fluid-structure interaction, the SPH particles for fluid domain and the DEM particles for solid domain are coupled together by using fluid-structure interaction under Newton's Third Law in which the forces on the solid from the fluid and the forces on the fluid from the solid are equal in magnitude but opposite in direction. The interaction forces between SPH particles and DEM particles follow Eq. (34). The density and the pressure for DEM particles stay unchanged at all times, and only their velocity and position evolve with time. It is worth noting that special care needs to be taken with the numerical technique when considering DEM particles in Eq. 25. For a structure composed of bonded DEM particles, the force from fluid to solid acts only on the surface layer of the structure, hence the inner DEM particles that are included in the support domain of a SPH particle should not be taken into account [69]. Even though this special technique is physically correct, the forces acting on the inner DEM particles are too small as they are close to the edge of support domain. Therefore, this technique is not used in this study yet and it will be undertaken in future to improve the coupled SPH-DEM model. The flow chart of coupling SPH and DEM is schematically described in Fig.16.
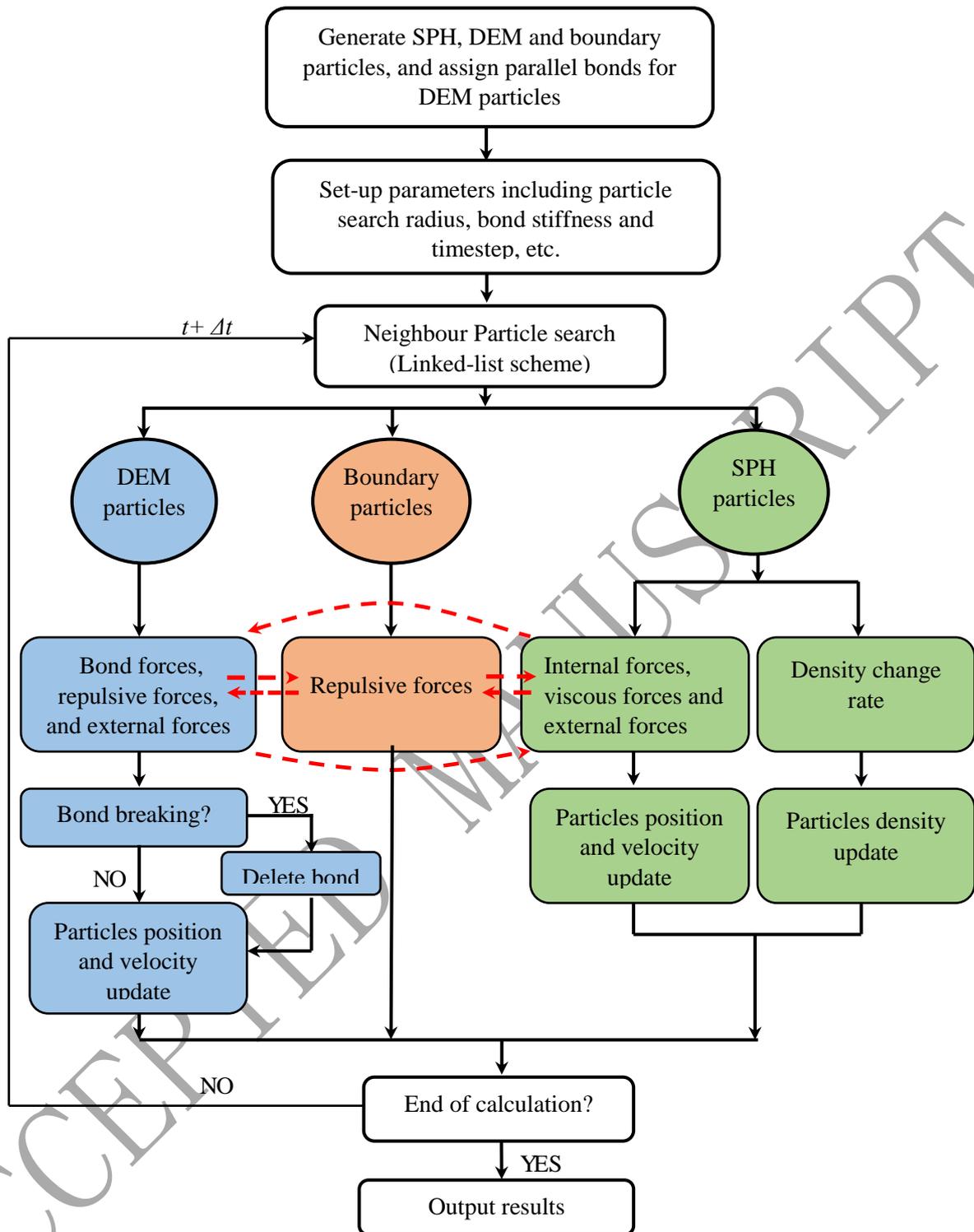
Fig.16 Computation flowchart for coupling DEM and SPH

4.2 Validation of the coupled SPH-DEM model

The validation test for the coupled SPH-DEM model is to simulate the water flow in the elastic gate problem for comparison with experimental data and numerical results using a coupled SPH-SPH method [11]. The initial configuration is illustrated in Fig.17 and the simulation parameters for this validation case are listed in Table 7. The top end of elastic gate in purple is fixed and the other end is

free to move. The bonded DEM particles representing the elastic gate are distributed in a hexagonal pattern and particle and bond stiffness is determined according to Eqs. (19-21) and (23). The SPH particles for water are initialised with hydrostatic pressure, and there is no pre-existing stress and deformation for bonded DEM particles.


- ● SPH particles
- ● DEM particles
- ● Boundary particles
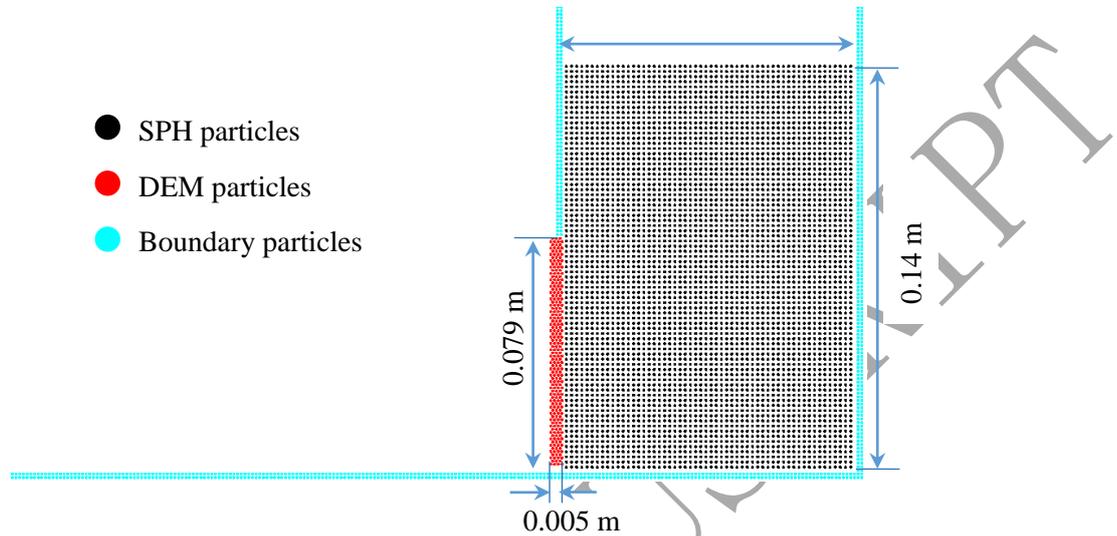
Fig.17 Configuration of 2D elastic gate test in a coupled SPH-DEM model

A comparison of numerical results from the present SPH-DEM model against experimental data and numerical results from the coupled SPH-SPH model is shown in Fig.18. Compared to the experiment snapshots, the deformation of the elastic plate and the vertical displacement of free surface of water are generally well predicted by the coupled SPH-DEM model. The maximum deformation of the plate is at top end and behaves almost as a rigid body without deformation at bottom end of the plate. It should be noted that after removing the hammer, which fixes the elastic plate against water pressure immediately in the experiment, water leakage besides the elastic plate is observed. Owing to this leakage, the water pressure acting on elastic plate is lower than that in the SPH-DEM simulation and consequently the vertical displacement of the free surface in the SPH-DEM simulation is larger than the experimental results. In comparison with both experimental and SPH-SPH results, both larger deformation and higher vertical displacement of the free surface in SPH-SPH and SPH-DEM results make sense without water leakage. Due to the decreasing hydrodynamic pressure of water, the deformation of the plate tends to be smaller after 0.16s in the SPH-DEM model, and as a result the vertical displacement of free surface changes more slowly.

Table.7 Parameters for SPH-DEM modelling of the elastic gate test

Parameters	Values
Boundary particle spacing (m)	0.00125
SPH particle spacing (m)	0.00175

DEM particle size (m)	0.00125
Particle number	6648
Kernel function type	Wendland
Kernel smooth length (m)	0.0021875
Fluid density (kg/m^3)	1000
Fluid viscosity (Pa$\cdot$s)	8.9×10^{-4}
Gate density (kg/m^3)	1100
Gate elastic modulus (MPa)	12.0
Gate Possoin's ratio	0.33
Time step (s)	0.000004
Physical time (s)	0.4

| Time	Experiment [11]	SPH-SPH [11]	SPH-DEM
(a) t=0.0s			
(b) t=0.08s			
(c) t=0.16s			
(d) t=0.24s			
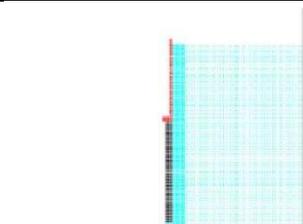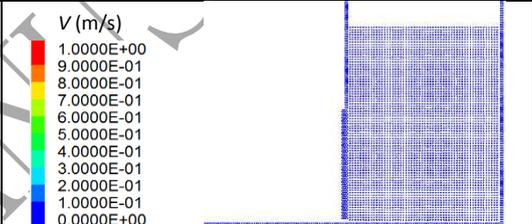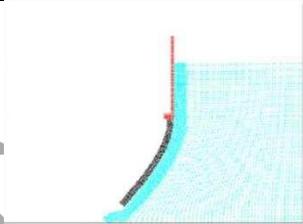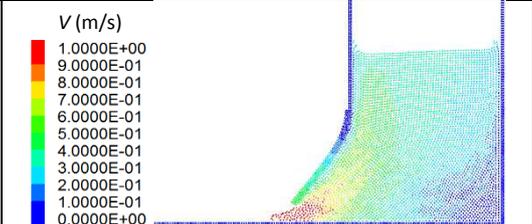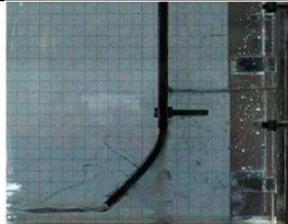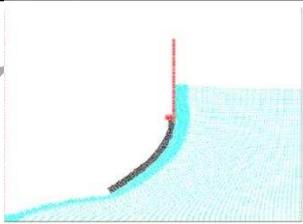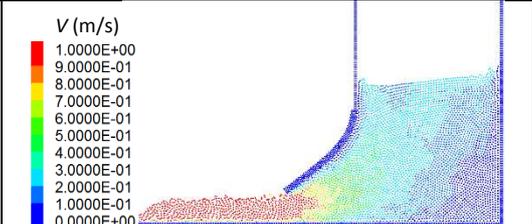
| (e) t=0.32s | | | |
| (f) t=0.40s | | | |
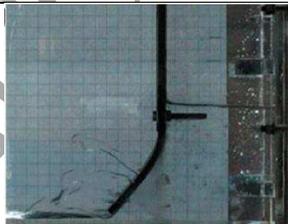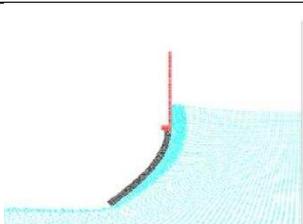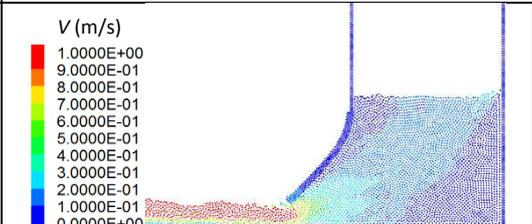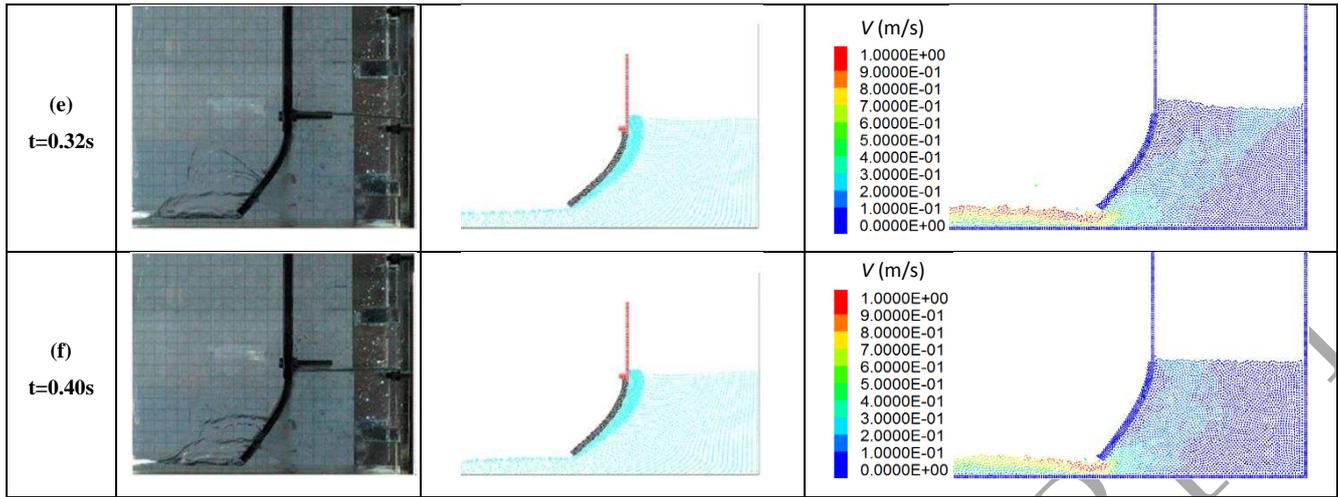
Fig.18 Comparisons between experimental, SPH-SPH and SPH-DEM results of elastic gate test with a time period of 0.40s.
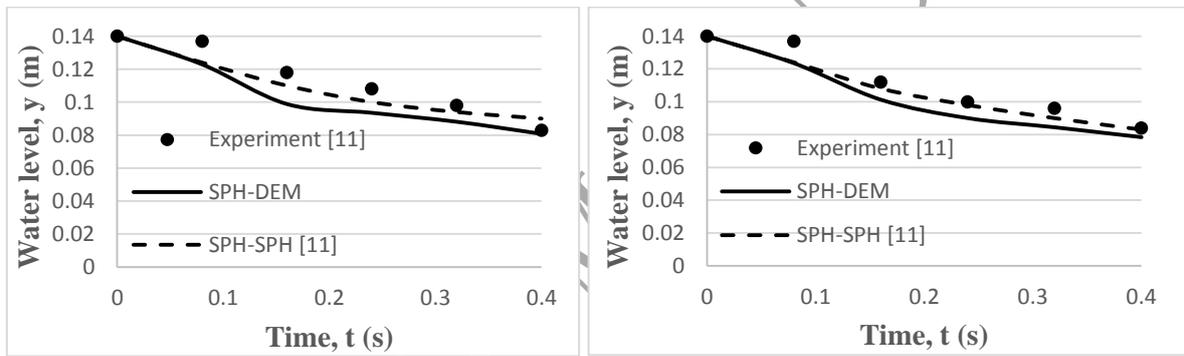
(a) Water level behind the gate   (b) Water level 5cm far from the gate

Fig.19 Water levels at different time

In Fig.119 the water levels behind the gate and the water level 5cm far from the gate are quantitatively recorded to represent the evolution of free surface with time. Due to the water leakage in the experiment, the flow rates calculated from both SPH-SPH and SPH-DEM models are slightly higher than the experimental data, which results in a faster decrease of water level. The SPH-SPH model and SPH-DEM model show good agreement throughout the entire test process in terms of plate deformation and vertical displacement of free surface.

5. Coupled SPH-DEM model for FSI with fracture

In order to demonstrate the versatility of the coupled SPH-DEM model in simulating fluid-structure interaction in this section, an FSI problem with fracture is presented. The same configuration in the validation test of coupled SPH-DEM model is used, as shown in Fig.20, but the elastic plate is clamped at the bottom end and free to move at the top end. In addition, the fixed plate in pink is removed in this case, and the material strength limit is lowered in order to allow for a fracture to occur

due to the pressure of the water. Simulation parameters in Table 7 are used here. In this case, the boundary particles not only produce repulsive forces to SPH particles but also need to respond to the fractured bonded DEM particles when they contact. As the momentum energy of fractured bonded DEM particles is much greater than an individual SPH particle, the two-layer boundary particles cannot produce large enough force to impede the penetration of fractured bonded DEM particles. To solve this issue, two different kinds of repulsive forces are created from every single boundary particle to act on the SPH particles and DEM particles, i.e., the smaller repulsive forces are only designated for SPH particles while fractured bonded DEM particles receive other greater repulsive forces.

In Fig.21 (a) and (b), the largest stress (stress component σ_{22}) is found near to the bottom end of elastic plate before the occurrence of fracture due to the maximum bending moment induced by the water pressure. At time around 0.12s, the strength limit of elastic plate is exceeded and consequently the elastic plate breaks into two parts and then the fractured part moves towards the left boundary wall under the forces produced by the SPH particles of water. With the modification of the boundary particles in handling the approaching bonded DEM particles, wall penetration is fully avoided. Due to the vibration of the elastic plate, the flow pattern of water is highly affected to cause flow fluctuation which leads to some irregular movements of certain individual particles or small clusters of particles. After 0.16s, the fractured structure is pushed away to approach the left solid boundary. When the plate moves along with bottom solid wall, the stresses acting on bond are negligible as no significant deformation is observed. This coupled SPH-DEM model used in FSI with fracture is not experimentally validated yet, but these results demonstrate its capabilities.
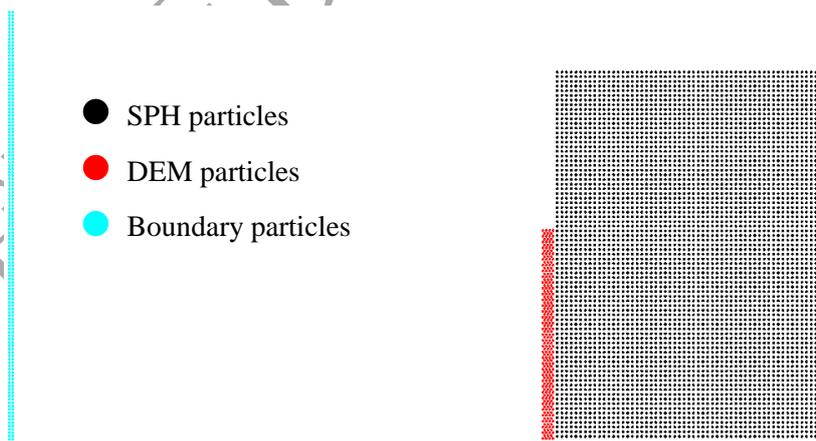

Fig.20 2D representation of FSI with fracture

Time	Particles velocity (m/s)	σ_{22} in the structure (Pa)

|		
(a) **t = 0.04s**		
(b) **t = 0.08s**		
(c) **t = 0.12s**		
(d) **t = 0.16s**		
(e) **t = 0.20s**		
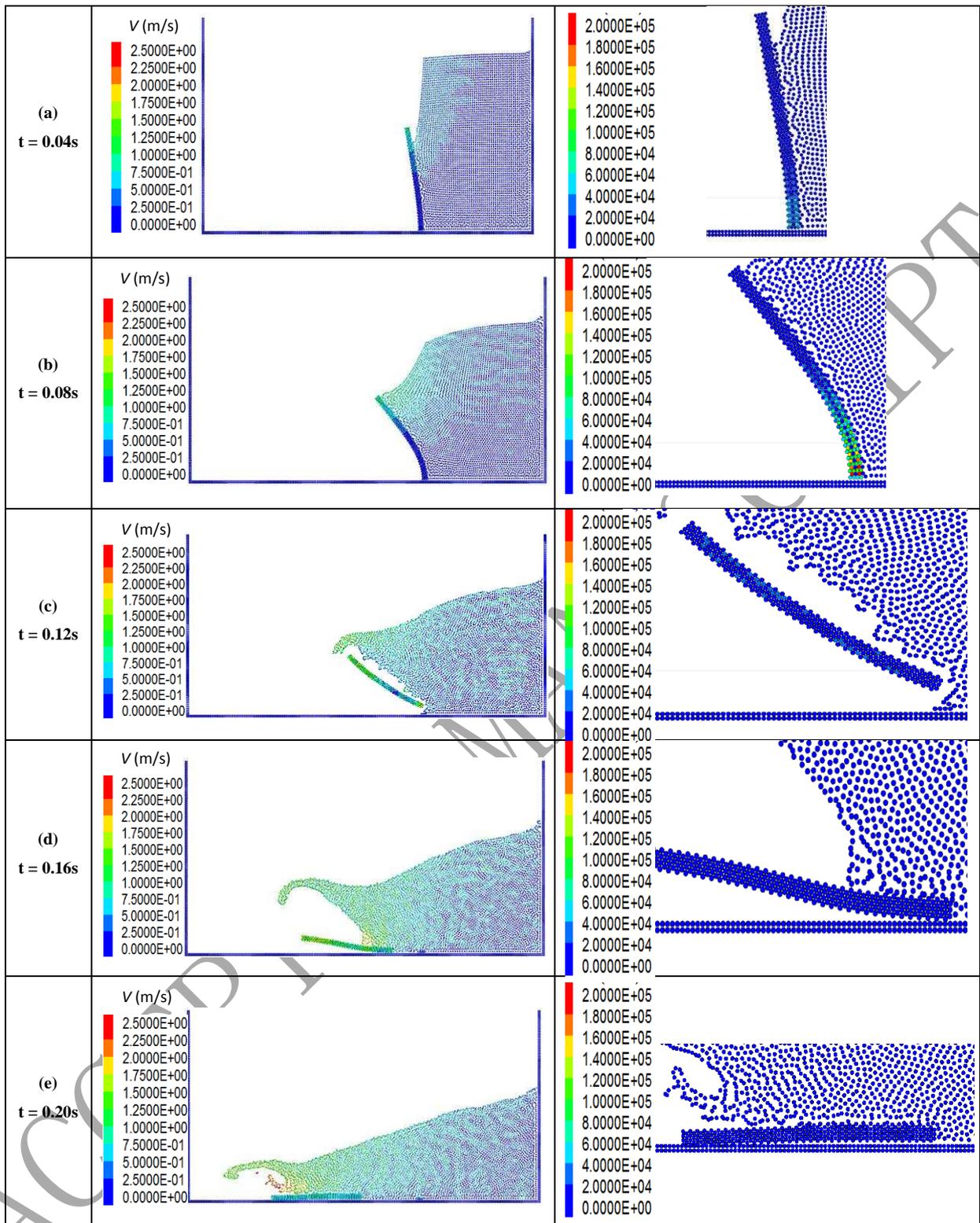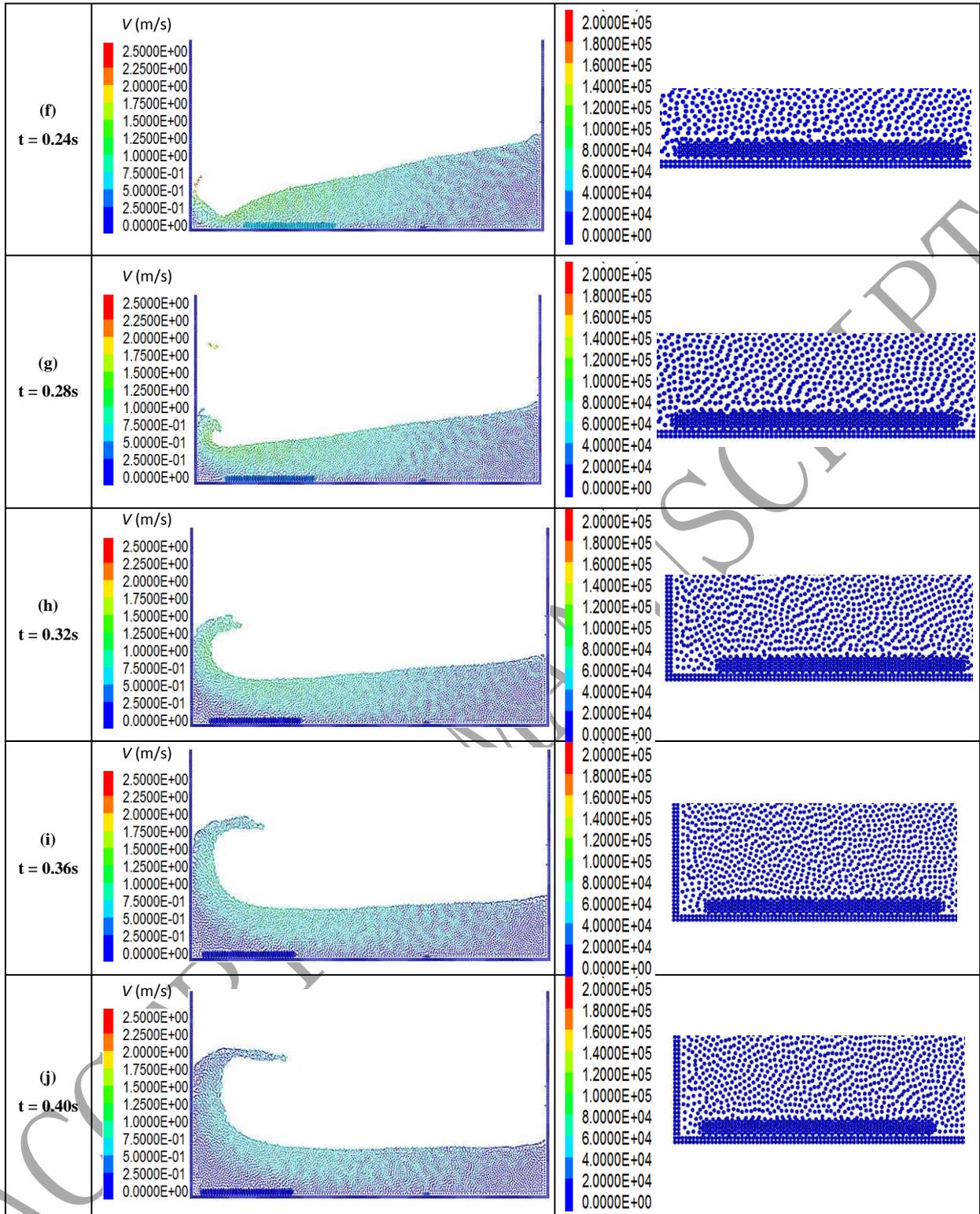
Fig.21 SPH-DEM modelling of FSI with fracture

6. Conclusions

A 2D coupled SPH-DEM model for fluid-structure interaction problems has been proposed and developed. In this model, SPH based on Navier-Stokes equations is used to model the fluid phase

while DEM with a bond feature is used for the solid phase. In dealing with the fluid-solid interface, Newton's Third Law is applied with the same magnitude in both phases, but in opposite directions. As both SPH and DEM are Lagrangian particle methods, no special treatment is required to define the fluid-structure interface, even in the presence of large deformation and/or fracture of structure. The contact between SPH and DEM particles is automatically detected in accordance with a particle search radius that is twice the smooth kernel length. When a smoothed particle is approaching a fixed boundary and its support domain is intersected with the boundary, two-layer boundary particles are placed in the position of solid boundary to produce repulsive forces to handle the kernel truncation.

The individual DEM model and SPH model has been validated by comparison with analytical, experimental and other numerical results. A tip-loaded cantilever beam has been chosen to validate the DEM model with bonded particles for predicting structural deformation and fracture. A typical dam-break test with dry bed was considered to validate the SPH model for predicting free surface flow. After the validations of both DEM and SPH models, the coupled SPH-DEM model was then validated against a typical fluid-structure interaction problem where a thin and long elastic plate interacts with free surface flowing fluid. Finally the coupled SPH-DEM model is extended to include the occurrence of structural fracture by allowing the bonds in the DEM model to break and the broken structure to move under fluid pressure.

The obtained results have shown satisfactory predictions in terms of flow pattern, structure deformation and velocity contour, although some improvements such as particle distribution density, no-slip condition, skin layer of solid structure, sensitivity studies in different kernel functions and smooth kernel lengths are still required. In the future, the coupled model will be expanded from 2D to 3D simulation. The case for fluid-structure interaction with fracture will be validated through laboratory experiment and further improvements for this coupled model will be made to enable the simulations of real engineering problems.

References

[1] Lee Y-J, Jhan Y-T, Chung C-H. Fluid–structure interaction of FRP wind turbine blades under aerodynamic effect. Composites Part B: Engineering. 2012;43:2180-91.

[2] Dubini G, Pietrabissa R, Montevecchi FM. Fluid-structure interaction problems in bio-fluid mechanics: a numerical study of the motion of an isolated particle freely suspended in channel flow. Medical Engineering & Physics. 1995;17:609-17.

[3] Peskin CS. Numerical analysis of blood flow in the heart. Journal of computational physics. 1977;25:220-52.

[4] Tang C-L, Hu J-C, Lin M-L, Angelier J, Lu C-Y, Chan Y-C, et al. The Tsaoling landslide triggered by the Chi-Chi earthquake, Taiwan: insights from a discrete element simulation. Engineering Geology. 2009;106:1-19.

[5] Nordbotten JM, Celia MA, Bachu S. Injection and storage of CO2 in deep saline aquifers: Analytical solution for CO2 plume evolution during injection. Transport in Porous media. 2005;58:339-60.

[6] Mirramezani M, Mirdamadi HR, Ghayour M. Innovative coupled fluid–structure interaction model for carbon nano-tubes conveying fluid by considering the size effects of nano-flow and nano-structure. Computational Materials Science. 2013;77:161-71.

[7] Nie X, Doolen GD, Chen S. Lattice-Boltzmann simulations of fluid flows in MEMS. Journal of Statistical Physics. 2002;107:279-89.

[8] Colagrossi A, Landrini M. Numerical simulation of interfacial flows by smoothed particle hydrodynamics. Journal of computational physics. 2003;191:448-75.

[9] Langston PA, Tüzün U, Heyes DM. Discrete element simulation of granular flow in 2D and 3D hoppers: dependence of discharge rate and wall stress on particle interactions. Chemical Engineering Science. 1995;50:967-87.

[10] Tan Y, Yang D, Sheng Y. Discrete element method (DEM) modeling of fracture and damage in the machining process of polycrystalline SiC. Journal of the European ceramic society. 2009;29:1029-37.

[11] Antoci C, Gallati M, Sibilla S. Numerical simulation of fluid–structure interaction by SPH. Computers & Structures. 2007;85:879-90.

[12] Ren B, Jin Z, Gao R, Wang Y-x, Xu Z-l. SPH-DEM Modeling of the Hydraulic Stability of 2D Blocks on a Slope. Journal of Waterway, Port, Coastal, and Ocean Engineering. 2013;140:04014022.

[13] Rabczuk T, Gracie R, Song J-H, Belytschko T. Immersed particle method for fluid-structure interaction. International Journal for Numerical Methods in Engineering. 2010;22:48.

[14] Rabczuk T, Belytschko T. A three-dimensional large deformation meshfree method for arbitrary evolving cracks. Computer Methods in Applied Mechanics and Engineering. 2007;196:2777-99.

[15] Han K, Feng YT, Owen DRJ. Numerical simulations of irregular particle transport in turbulent flows using coupled LBM-DEM. Computer Modeling in Engineering and Sciences. 2007;18:87.

[16] Dunne T. An Eulerian approach to fluid‐structure interaction and goal‐oriented mesh adaptation. International journal for numerical methods in fluids. 2006;51:1017-39.

[17] Takagi S, Sugiyama K, Ii S, Matsumoto Y. A review of full Eulerian methods for fluid structure interaction problems. Journal of Applied Mechanics. 2012;79:010911.

[18] Ahmed S, Leithner R, Kosyna G, Wulff D. Increasing reliability using FEM–CFD. World Pumps. 2009;2009:35-9.

[19] Kim S-H, Choi J-B, Park J-S, Choi Y-H, Lee J-H. A coupled CFD-FEM analysis on the safety injection piping subjected to thermal stratification. Nuclear Engineering and Technology. 2013;45:237-48.

[20] Peksen M. 3D transient multiphysics modelling of a complete high temperature fuel cell system using coupled CFD and FEM. International Journal of Hydrogen Energy. 2014;39:5137-47.

[21] Peksen M, Peters R, Blum L, Stolten D. 3D coupled CFD/FEM modelling and experimental validation of a planar type air pre-heater used in SOFC technology. International Journal of Hydrogen Energy. 2011;36:6851-61.

[22] Hou G, Wang J, Layton A. Numerical methods for fluid-structure interaction—a review. Commun Comput Phys. 2012;12:337-77.

[23] Blocken B, Stathopoulos T, Carmeliet J. CFD simulation of the atmospheric boundary layer: wall function problems. Atmospheric Environment. 2007;41:238-52.

[24] Lee N-S, Bathe K-J. Error indicators and adaptive remeshing in large deformation finite element analysis. Finite Elements in Analysis and Design. 1994;16:99-139.

[25] Liu G-R, Liu MB. Smoothed particle hydrodynamics: a meshfree particle method: World Scientific; 2003.

[26] De Rosis A, Falcucci G, Ubertini S, Ubertini F. A coupled lattice Boltzmann-finite element approach for two-dimensional fluid–structure interaction. Computers & Fluids. 2013;86:558-68.

[27] Haddad H, Guessasma M, Fortin J. Heat transfer by conduction using DEM–FEM coupling method. Computational Materials Science. 2014;81:339-47.

[28] Canelas RB, Crespo AJC, Domínguez JM, Ferreira RML, Gómez-Gesteira M. SPH–DCDEM model for arbitrary geometries in free surface solid–fluid flows. Computer Physics Communications. 2016;202:131-40.

[29] Robinson M, Ramaioli M, Luding S. Fluid–particle flow simulations using two-way-coupled mesoscale SPH–DEM and validation. International journal of multiphase flow. 2014;59:121-34.

[30] Birnbaum NK, Francis NJ, Gerber BI. Coupled techniques for the simulation of fluid-structure and impact problems. Computer Assisted Mechanics and Engineering Sciences. 1999;6:295-311.

[31] Rafiee A, Thiagarajan KP. An SPH projection method for simulating fluid-hypoelastic structure interaction. Computer Methods in Applied Mechanics and Engineering. 2009;198:2785-95.

[32] Fries TP. A corrected XFEM approximation without problems in blending elements. International Journal for Numerical Methods in Engineering. 2008;75:503-32.

[33] Zi G, Belytschko T. New crack‐tip elements for XFEM and applications to cohesive cracks. International Journal for Numerical Methods in Engineering. 2003;57:2221-40.

[34] Vu-Bac N, Nguyen-Xuan H, Chen L, Lee C-K, Zi G, Zhuang X, et al. A phantom-node method with edge-based strain smoothing for linear elastic fracture mechanics. Journal of Applied Mathematics. 2013;2013.

[35] Cai Y, Zhu H, Zhuang X. A continuous/discontinuous deformation analysis (CDDA) method based on deformable blocks for fracture modeling. Frontiers of Structural and Civil Engineering. 2013;7:369-78.

[36] Zhuang X, Augarde CE, Mathisen KM. Fracture modeling using meshless methods and level sets in 3D: framework and modeling. International Journal for Numerical Methods in Engineering. 2012;92:969-98.

[37] Rabczuk T, Zi G. A meshfree method based on the local partition of unity for cohesive cracks. Computational Mechanics. 2007;39:743-60.

[38] Rabczuk T, Areias PMA, Belytschko T. A meshfree thin shell method for non‐linear dynamic fracture. International Journal for Numerical Methods in Engineering. 2007;72:524-48.

[39] Tan Y, Zhang H, Yang D, Jiang S, Song J, Sheng Y. Numerical simulation of concrete pumping process and investigation of wear mechanism of the piping wall. Tribology International. 2012;46:137-44.

[40] Yang D, Sheng Y, Ye J, Tan Y. Discrete element modeling of the microbond test of fiber reinforced composite. Computational materials science. 2010;49:253-9.

[41] Tavarez FA, Plesha ME. Discrete element method for modelling solid and particulate materials. International Journal for Numerical Methods in Engineering. 2007;70:379-404.

[42] Cundall PA, Strack ODL. A discrete numerical model for granular assemblies. Geotechnique. 1979;29:47-65.

[43] Itasca Consulting Group I. PFC 5.0 documentation. 2011.

[44] Itasca Consulting Group I. PFC – Particle Flow Code. 2014.

[45] Mindlin RD, Deresiewica H. Elastic spheres in contact under varying oblique forces. Journal of Applied Mechanics. 2014;20.

[46] Potyondy DO, Cundall PA. A bonded-particle model for rock. International journal of rock mechanics and mining sciences. 2004;41:1329-64.

[47] Yang D, Sheng Y, Ye J, Tan Y. Dynamic simulation of crack initiation and propagation in cross-ply laminates by DEM. Composites Science and Technology. 2011;71:1410-8.

[48] McGuire W, Gallagher RH, Ziemian RD. Matrix structural analysis2000.

[49] Gingold RA, Monaghan JJ. Smoothed particle hydrodynamics: theory and application to non-spherical stars. Monthly notices of the royal astronomical society. 1977;181:375-89.

[50] Cleary PW. Modelling confined multi-material heat and mass flows using SPH. Applied Mathematical Modelling. 1998;22:981-93.

[51] Monaghan JJ, Kocharyan A. SPH simulation of multi-phase flow. Computer Physics Communications. 1995;87:225-35.

[52] Monaghan JJ. Simulating free surface flows with SPH. Journal of computational physics. 1994;110:399-406.

[53] Monaghan JJ, Lattanzio JC. A refined particle method for astrophysical problems. Astronomy and Astrophysics. 1985;149:135-43.

[54] Wendland H. Piecewise polynomial, positive definite and compactly supported radial functions of minimal degree. Advances in computational Mathematics. 1995;4:389-96.

[55] Chen JK, Beraun JE, Carney TC. A corrective smoothed particle method for boundary value problems in heat conduction. International Journal for Numerical Methods in Engineering. 1999;46:231-52.

[56] Monaghan JJ. Smoothed particle hydrodynamics. Reports on progress in physics. 2005;68:1703.

[57] Morris JP, Fox PJ, Zhu Y. Modeling low Reynolds number incompressible flows using SPH. Journal of computational physics. 1997;136:214-26.

[58] Morris JP, Monaghan JJ. A switch to reduce SPH viscosity. Journal of Computational Physics. 1997;136:41-50.

[59] Randles PW, Libersky LD. Smoothed particle hydrodynamics: some recent improvements and applications. Computer Methods in Applied Mechanics and Engineering. 1996;139:375-408.

[60] Dyka CT, Randles PW, Ingel RP. Stress points for tension instability in SPH. International Journal for Numerical Methods in Engineering. 1997;40:2325-41.

[61] Randles PW, Libersky LD. Normalized SPH with stress points. International Journal for Numerical Methods in Engineering. 2000;48:1445-62.

[62] Monaghan JJ. SPH without a tensile instability. Journal of computational physics. 2000;159:290-311.

[63] Kajtar JB. Smooth lattice general relativity, and SPH simulations of swimming linked bodies. 2010.

[64] Koshizuka S, Oka Y. Moving-particle semi-implicit method for fragmentation of incompressible fluid. Nuclear science and engineering. 1996;123:421-34.

[65] Jánosi IM, Jan D, Szabó KG, Tél T. Turbulent drag reduction in dam-break flows. Experiments in Fluids. 2004;37:219-29.

[66] Koshizuka S, Oka Y, Tamako H. A particle method for calculating splashing of incompressible viscous fluid. American Nuclear Society, Inc., La Grange Park, IL (United States); 1995.

[67] Huang YJ, Nydal OJ. Coupling of discrete-element method and smoothed particle hydrodynamics for liquid-solid flows. Theoretical and Applied Mechanics Letters. 2012;2:012002.

[68] Sun F. Investigations of smoothed particle hydrodynamics method for fluid-rigid body interactions. 2013.

[69] Paredes RJ, Imas L. Application of Multiphase SPH to Fluid Structure Interaction Problems.